Probing a Novel Antibiotic Target in

Pseudomonas aeruginosa

Submitted by

Jarrod L Kubsch-Bermingham

Bachelor of Biological Science, 2019

This thesis is submitted in total fulfillment of the requirements for the degree of

Master of Science

School of Molecular Sciences

College of Science, Health and Engineering

La Trobe University

Victoria, Australia

September 2021

Table of Contents

List of Figures

List of Tables

COVID-19 Impact Statement

COVID-19 severely restricted my laboratory-based research time. The project, which was initially designed to be completed over approximately 16 months, has been condensed into 9 months – three of which were limited to 20-hours of laboratory access per week. The time constraints on laboratory-based research have particularly impacted my project as no dry research could be conducted to complete its aims. Moreover, completion of some of my experiments required full days of laboratory access, hence during the 3 months of restricted access, I was limited to 2 days per week to meet the time limit restrictions. This severely restricted the amount of work performed as my experiments often required consecutive days of bacterial incubation. The unpredictability of the lockdowns also limited the opportunity to plan long-term experiments. Given these factors, aspects of the project were not completed to the same degree as initially planned.

Abstract

Antibiotic resistance represents one of the greatest threats to global health. A high priority antibiotic-resistant bacteria that requires the urgent development of new antibiotics is *Pseudomonas aeruginosa*. One strategy to overcome resistance in this pathogen is to identify novel antibiotic targets. Accordingly, this thesis focuses on the enzyme diaminopimelate epimerase (DAPEP) within the diaminopimelate (DAP) pathway. DAPEP is responsible for the interconversion of L,L-DAP to *meso*-DAP, which is used in the crosslinking of peptidoglycan in the bacterial cell wall. This project aims to investigate DAPEP as a novel antibiotic target in *P. aeruginosa*, employing (i) kinetic and (ii) structural techniques, and (iii) by characterising the effect of *meso*-DAP depletion on bacterial survival. To recombinantly produce the enzyme from *P. aeruginosa*, a pET28a-*dapF* expression vector was designed and cloned, and *P. aeruginosa* (Pa) DAPEP was expressed and purified to yield milligram quantities at ~99% purity. Steady-state kinetics was employed to determine the binding affinity of PaDAPEP for L,L-DAP of 0.14 ± 0.03 mM, while the catalytic turnover was determined to be 127 ± 6 s^{-1}. In solution characterisation was performed using circular dichroism spectroscopy and analytical ultracentrifugation, indicating that PaDAPEP adopts a predominantly β-structure dimeric conformation. Using X-ray crystallography, the structure of PaDAPEP was solved to 1.7 Å, allowing the identification of potential inhibition sites to guide future structure-based drug discovery. To characterise *meso*-DAP depletion in bacteria, a direct deletion of the PaDAPEP encoding gene was pursued. A suicide vector was successfully cloned, and transformation conditions were extensively optimised to allow the generation of a deletion mutant in the future. In summary, this thesis provides the initial steps towards developing a tool to characterise *meso*-DAP depletion in *P. aeruginosa*, and its findings have provided insights into the structure and catalytic parameters of PaDAPEP that will provide the framework for developing novel classes of antibacterial agents.

Statement of Authorship

Except where reference is made in the text of the thesis, this thesis contains no other material published elsewhere or extracted in whole or in part from a thesis accepted for the award of any other degree or diploma. No other person's work has been used without due acknowledgement in the main text of the thesis. This thesis has not been submitted for the award of any degree or diploma in any other tertiary institution.

Jarrod Kubsch-Bermingham

27th September 2021

Abbreviations

AUC	Analytical ultracentrifugation
CD	Circular dichroism
CDC	Centers for Disease Control and Prevention
CE	Crude extract
Cg	*Corynebacterium glutamicum*
CL	Crude lysate
DAP	Diaminopimelate
DAPEP	Diaminopimelate epimerase
GNB	Gram-negative bacteria
GPB	Gram-positive bacteria
h	Hours
Hi	*Haemophilus influenzae*
IMAC	Immobilised metal affinity chromatography
IPTG	Isopropyl-β-D-thiogalactoside
K_{cat}	Catalytic turnover
K_m	Michaelis-Menten constant
LB	Luria-Bertani
MDR	Multi drug-resistant
min	Minutes
NAG	N-acetylglucosamine
NAM	N-acetylmuramic acid
NEB	New England Biolabs
OD_{600}	Optical density at 600 nm

OM	Outer membrane
Pa	*Pseudomonas aeruginosa*
PDR	Pan drug-resistant
PEG	Polyethylene glycol
PISA	Proteins, Interfaces, Structures, and Assemblies
RMSD	Root-mean-square deviation
RND	Resistance-nodulation-division
s	Seconds
SDS-PAGE	Sodium dodecyl sulfate-polyacrylamide gel electrophoresis
TLS	Translation/Liberation/Screw
TSA	Tryptic soy agar
U.S.	United States
v/v	Volume per volume
V_{max}	Maximal rate of an enzyme
w/v	Weight per volume
WHO	World Health Organization
XDR	Extensively drug-resistant

Acknowledgments

Completing this thesis was certainly an adventure with many ups and downs. However, through it all, I've had unwavering support and guidance from numerous people who have helped make this journey much more bearable.

First and foremost, I would like to extend my deepest gratitude to my supervisor Dr Tatiana Soares da Costa for her support, patience, and mentorship throughout my time in the lab. Tatiana, the passion and excitement you bring to science has been the single most motivating factor for me and has inspired me to pursue a research career. You have imparted invaluable skills and wisdom upon me that I am sure I will use for years to come in all facets of life – thank you!

Thanks should also go to past and present members of the lab for their friendship, advice, and all the laughs. Dan, Em, Ryan, Jess, Sreshtha, Seb, Rach, and Cody, I am so grateful for every time one of you have sacrificed your own time to assist me, and for that I am indebted to you all. It has been a difficult couple of years for everyone, however, the office chats, hours spent in the tearoom and general positive outlook has made my time in the lab so much more enjoyable.

Finally, I would like to thank Sam and my family. The love and support I have received, from you all, has been so important for me. I am incredibly lucky to have you all by my side and could not be more grateful.

Chapter One

Introduction

1.1   The Need for Antibiotics

The discovery of penicillin by Sir Alexander Fleming in 1928 marked the beginning of the 'golden era' of antibiotics (Aminov, 2010). The years following Fleming's discovery, up until the late 1960s, saw the introduction of 12 out of the 14 antibiotic classes that are currently in use (Conly & Johnston, 2005). Most of our antibiotics target five major cellular processes in bacteria, namely cell wall synthesis, protein biosynthesis, nucleic acid replication, membrane structure and folic acid metabolism (Kapoor *et al*, 2017; Sengupta *et al*, 2013). The success of antibiotics targeting these processes has resulted in a means of reducing mortality that is unmatched in the history of medical pharmacotherapy (Spellberg & Gilbert, 2014). As such, modern medicine has become heavily reliant on effective antibiotics, with many medical procedures, including common surgeries, organ transplants and cancer chemotherapy, not being possible without antibiotic intervention (Hutchings *et al*, 2019; Spellberg & Gilbert, 2014). Despite our reliance on effective antibiotics, there has been a significant reduction in their research and development due to a low return on investment for pharmaceutical companies (Renwick & Mossialos, 2018). The problem is further compounded by various scientific and regulatory barriers, such as the difficulty of identifying new targets and strict

procedures imposed by regulatory agencies (Spellberg & Gilbert, 2014; Ventola, 2015). The lack of research and development has resulted in a 30-year antibiotic discovery void that poses a significant threat to public health, as current antibiotics are becoming less effective due to increasing levels of resistance.

1.1.1 The Emergence of Antibiotic Resistance

Accompanying the discovery of penicillin were predictions from Fleming himself about the development of antibiotic resistance (Rosenblatt-Farrell, 2009). These predictions were eventually realised, and antibiotic resistance is now rising to dangerously high levels. The main cause of this increase has been the misuse and overuse of commercially available antibiotics in humans, as data has indicated that at least 30% of antibiotic prescriptions are unnecessary (Fleming-Dutra *et al*, 2016). This is thought to be exacerbated by the prophylactic use of antibiotics in animal agriculture, which has been found to accelerate the development of resistant bacteria and lead to cross-species transmission of resistant pathogens via meat products, direct contact and shared resources such as contaminated water (Landers *et al*, 2012; Van Boeckel *et al*, 2019). An alarming increase in clinical resistance has also been observed as multi drug-resistant (MDR), extensively drug-resistant (XDR) and pan drug-resistant (PDR) pathogens – the latter being resistant to all current antibiotic classes – are becoming more prevalent (Magiorakos *et al*, 2012; Ventola, 2015). These pathogens have already placed a significant burden on healthcare systems around the world, resulting in longer hospital admissions and higher morbidity and mortality. Furthermore, it is estimated that 700,000 deaths per year can be attributed to antimicrobial resistance (Friedman *et al*, 2016; World Health Organisation, 2014; O'Neill, 2014). The annual economic impact associated with healthcare and productivity losses has been estimated to be $55 billion in the United States (U.S.) alone (Centers for Disease Control and Prevention, 2013). If left unchecked, resistance to antibiotics

has been predicted to reduce the world's GDP by 100 trillion USD and result in 10 million fatalities annually by the year 2050 (O'Neill, 2014). Accordingly, public health organisations, such as the World Health Organization (WHO) and the Centers for Disease Control and Prevention (CDC), have compiled reports that identify the highest-priority resistant pathogens and make recommendations for research prioritisation (Centers for Disease Control and Prevention, 2019; World Health Organisation, 2014). One of the highest-priority bacteria that require the urgent development of new antibiotics is *Pseudomonas aeruginosa.*

1.2 *Pseudomonas aeruginosa*

P. aeruginosa is a Gram-negative bacteria (GNB) known to inhabit an extensive array of ecological niches, including soil, organic matter, skin flora, water and medical equipment (Lister *et al*, 2009). Commonly classified as opportunistic pathogens, *P. aeruginosa* target those who are immunocompromised and are one of the leading causes of nosocomial infections worldwide (Bassetti *et al*, 2018). *P. aeruginosa* infections are most notably implicated in patients with cystic fibrosis and are the major cause of morbidity and mortality for the disease (Behrends *et al*, 2013). This arises from the difficulty of treating *P. aeruginosa* infections resulting from the various chromosomally encoded mechanisms the bacteria possess, which will be discussed in Section 1.2.1 (Meletis & Bagkeri, 2013). Accordingly, a standard antibiotic therapy for *P. aeruginosa* infections typically combines two agents from different antibiotic classes, creating a 'double coverage effect' that aims to improve potency and provides the best chance for successful treatment (Bassetti *et al*, 2018). The most frequently used antibiotics in these therapies belong to the aminoglycoside, quinolone and beta-lactam classes (Meletis & Bagkeri, 2013). However, *P. aeruginosa* are infamous for their propensity to adaptively generate resistance even to these combinatorial treatments, resulting in MDR, XDR and PDR strains (Bassetti *et al*, 2018). In fact, in the U.S., 14% of *P. aeruginosa* isolates were classified

as MDR strains, as they were found to display resistance to three or more antibiotic classes (Nguyen *et al*, 2018). These highly resistant strains are treated on a case-by-case basis and often rely on 'last resort' options such as carbapenems, 3rd generation cephalosporins and polymyxins (Bassetti *et al*, 2018; Nguyen *et al*, 2018). Critically, reports of resistance to these last resort treatments are becoming more frequent (Nguyen *et al*, 2018).

1.2.1   *P. aeruginosa* Resistance Mechanisms

MDR *P. aeruginosa* often exhibit a combination of acquired and chromosomally encoded resistance mechanisms, in addition to various mutations that lead to the overexpression of genes that express resistance mechanisms (Lister *et al*, 2009). Being a GNB, the structure of its cell wall provides the first layer of resistance to antibiotics. As opposed to Gram-positive bacteria (GPB), GNB have an extra lipid bilayer on the outside of the peptidoglycan cell wall that forms an outer membrane (OM) (Figure 1A) (Beveridge, 2001). The presence of this OM makes all GNB inherently impermeable to some antibiotics and is the reason why large drugs that are effective against GPB, such as vancomycin, have no efficacy towards GNB (Munita & Arias, 2016).

Additionally, water filled pores known as porins, which are found on the OM, can generate resistance by selectively decreasing the permeability of the cell wall (Figure 1A) (Kapoor *et al*, 2017; Munita & Arias, 2016). Typically, porins facilitate the passive diffusion of small biomolecules to the cytoplasmic membrane, transporting nutrients and substrates into the cell, and contaminants and waste out (Welte *et al*, 1995). However, upon antibiotic exposure, alterations to porin expression can occur, conferring resistance to that antibiotic (Munita & Arias, 2016). One of the most well-characterised mechanisms of porin-mediated resistance in *P. aeruginosa* is the in-frame deletion of loop 7 of the OprD porin, which generates resistance

to carbapenems, whilst retaining its endogenous ability to transport basic amino acids (Kos *et al*, 2016).

The cell wall also facilitates the activity of integral membrane proteins called efflux pumps, which can actively extrude toxins and antimicrobials from the bacterial cytoplasm (Figure 1A) (Venter *et al*, 2015). Efflux pump-mediated antibiotic resistance in *P. aeruginosa* is governed by four main efflux systems from the resistance-nodulation-division superfamily, and includes MexAB-OprM, MexCD-OprJ, MexEF-OprN and MexXY-OprM (Bassetti *et al*, 2018). Overexpression of these efflux pumps due to antibiotic pressure is collaboratively able to generate resistance to every antibiotic class, excluding polymyxins as their mode of action does not require entry into the cell (Bassetti *et al*, 2018; Falagas *et al*, 2005; Kapoor *et al*, 2017).

P. aeruginosa are also well known for their intrinsic ability to form protective biofilms (Figure 1B) (Mielko *et al*, 2019). These biofilms form on a surface, whereby bacteria aggregate and adhere to each other to produce a dense matrix of extracellular biomolecules, such as proteins, exopolysaccharides and metabolites (Pang *et al*, 2019). Formation of these biofilms allows for greatly increased persistence from host and antibiotic attack, whilst also allowing for metabolite exchange and horizontal gene transfer, providing an ideal environment for the survival and maturation of *P. aeruginosa* (dos Santos *et al*, 2018; Moradali *et al*, 2017) Regulation of these biofilms is primarily governed via quorum sensing, which is a complex communication system for bacteria that allows them to coordinate gene expression in accordance with local population density (Swift *et al*, 1996). While it does assist with biofilm maintenance, quorum sensing contributes to the pathogenesis of *P. aeruginosa* through the regulation of various virulence factors (Venturi, 2006). Thus, it is evident that we urgently need to develop new antibiotics that can overcome these resistance mechanisms. A previously validated cellular process that may harbour new antibiotic targets is cell wall biosynthesis.
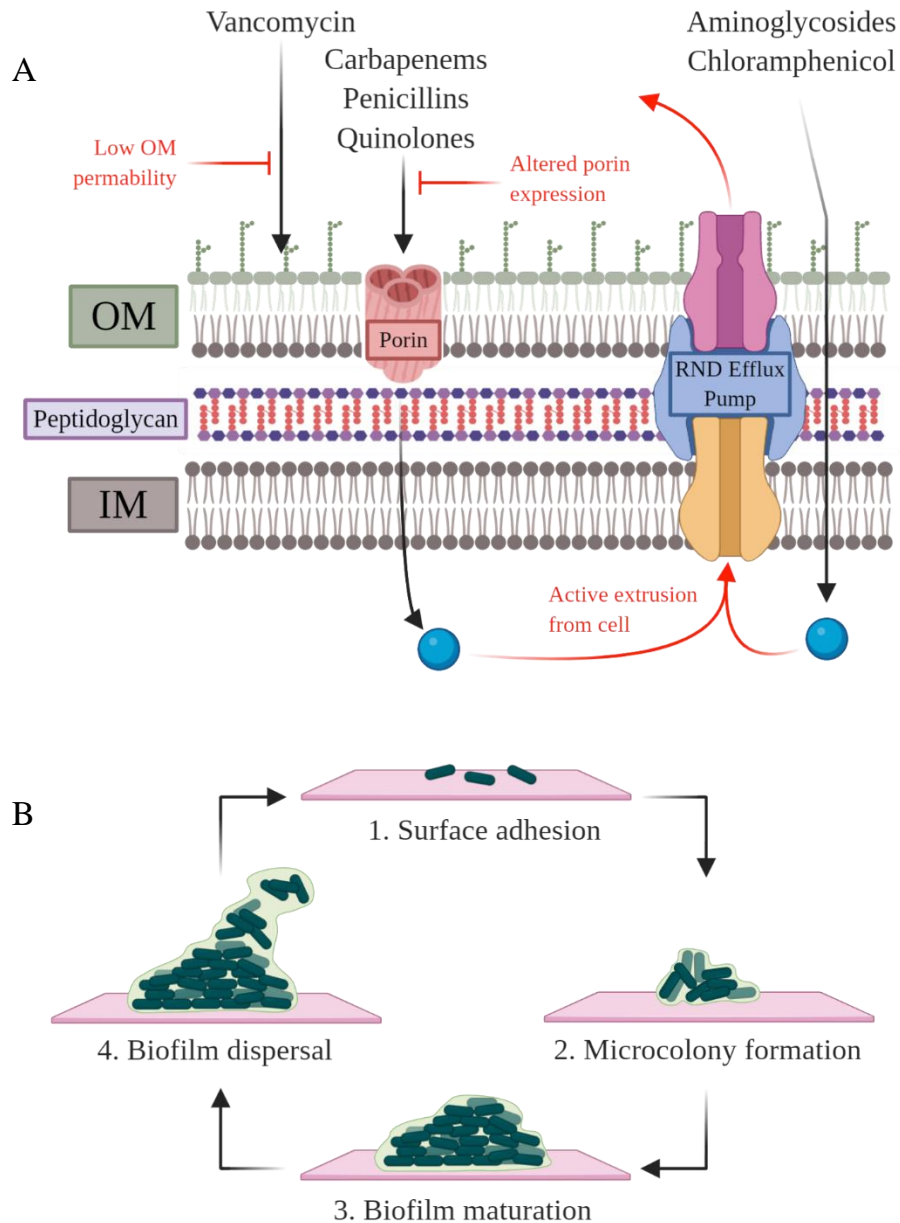
Figure 1. *P. aeruginosa* resistance mechanisms. (A) The cell wall of *P. aeruginosa* facilitates several resistance mechanisms, including the exclusion of larger drugs by the outer membrane (OM), alterations to porin expression and active extrusion of antibiotics from the cell via resistance-nodulation-division (RND) efflux pumps. **(B)** Biofilm formation is a cyclic process that occurs in 4 steps: (1) adhesion of planktonic *P. aeruginosa* to a solid surface; (2) extracellular matrix is produced and a multilayered microcolony forms; (3) further bacterial growth and formation of complex matrix; (4) matured planktonic bacteria are dispersed and the process repeats. Adapted from Landini *et al*. (2010).

1.3 Targeting Cell Wall Biosynthesis

As previously discussed, the cell wall of *P. aeruginosa* promotes several antibiotic resistance mechanisms. Its principal function, however, is to protect the intracellular contents of bacteria and preserve cell integrity by maintaining rigidity (Silhavy *et al*, 2010; Vollmer *et al*, 2008). Hence, the biosynthesis of the cell wall is an essential process for the survival of bacteria, which in addition to its absence in eukaryotic cells, makes it an ideal target for clinical exploitation (Sarkar *et al*, 2017). Cell wall biosynthesis pathways are well characterised, facilitating the development of many antibiotics that inhibit the pathway. More specifically, these antibiotics focus on disrupting the synthesis and assembly of the peptidoglycan (Figure 2). The peptidoglycan is a component of the bacterial cell wall responsible for withstanding turgor pressure and maintaining the shape of the cell, whilst also serving as an anchoring point for membrane proteins and other cell wall components (Vollmer *et al*, 2008). It consists of an assembly of repeating subunits containing N-acetylglucosamine (NAG) and N-acetylmuramic acid (NAM) residues linked through a glycosidic bond (Margolin, 2018). These disaccharide monomers are cross-linked by pentapeptides attached to each NAM residue, consisting of an L-Ala–D-Glu–L-Lys–D-Ala–D-Ala sequence in GPB and an L-Ala–D-Glu–*meso*-DAP–D-Ala–D-Ala sequence in GNB (Margolin, 2018; Vollmer *et al*, 2008). Several classes of antibiotics already target these linking peptides, most notably beta-lactams and glycopeptides. Betalactams inhibit the cross-linking of the disaccharide monomers by binding to a family of membrane-associated enzymes named penicillin-binding proteins (Sarkar *et al*, 2017). On the other hand, glycopeptide classed antibiotics bind to the D-Ala–D-Ala moiety of the pentapeptide, which weakens the peptidoglycan, leading to cell lysis due to turgor pressure (Sarkar *et al*, 2017). Beta-lactams and glycopeptides are two of the most widely used antibiotic classes, demonstrating proof of concept for antibiotics targeting constituents of the

peptidoglycan. One constituent that remains under-exploited is *meso*-diaminopimelate (DAP), found within the linking pentapeptide in GNB.
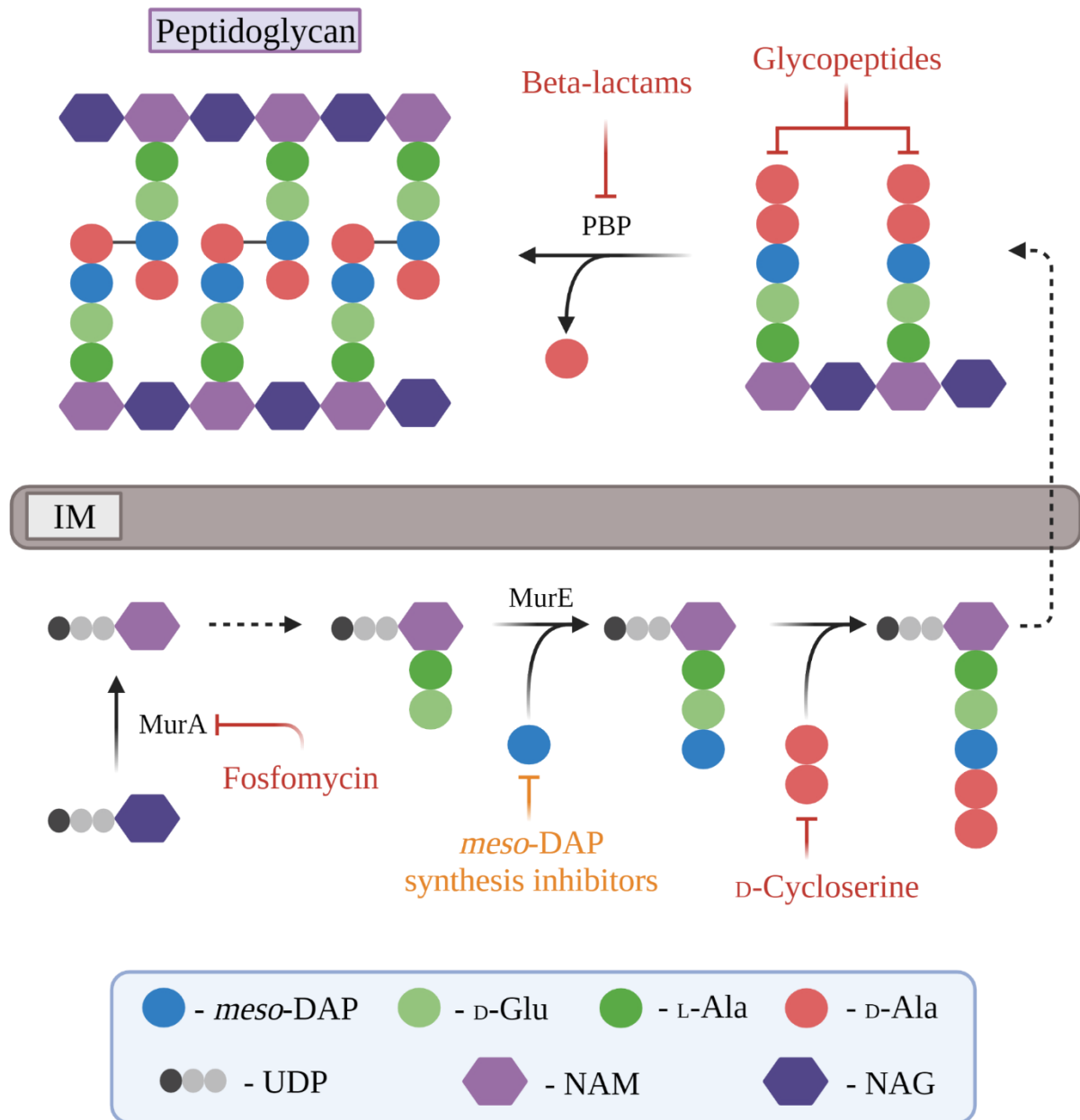
Figure 2. Peptidoglycan biosynthesis inhibitors. There are several peptidoglycan biosynthesis inhibitors available on the market, including fosfomycin, cycloserine, betalactams and glycopeptides. Beta-lactam and fosfomycin classed antibiotics bind to enzymes found within the pathway inhibiting the production of peptidoglycan precursors. Glycopeptides bind to the D-Ala–D-Ala moiety of the penicillin-binding-protein (PBP) substrate, preventing the cross-linking of the linear peptidoglycan chains. Cycloserine antibiotics prevent the downstream production of the D-Ala–D-Ala dipeptide by inactivating the alanine racemase and D-Ala–D-Ala ligase responsible for its production. Inhibitors of the synthesis of *meso*diaminopimelate (DAP) would follow a similar mechanism, inactivating DAP epimerase – the enzyme that catalyses the production of *meso*-DAP. Adapted from Sarkar *et al*. (2017).

1.4   Diaminopimelate

The metabolite *meso*-DAP is produced via a reaction catalysed by the enzyme DAP epimerase (DAPEP) within the DAP pathway (Dogovski *et al*, 2009). Inhibition of *meso*-DAP biosynthesis remains a largely unexplored avenue in antibiotic discovery, despite being a key metabolite in the peptidoglycan of GNB. In fact, the importance of *meso*-DAP on the viability of GNB remains unknown. Moreover, the DAP pathway is also responsible for the production of L-lysine (hereafter referred to as lysine), which is critical for protein production (Hutton *et al*, 2007). Therefore, antibiotics targeting DAPEP would concurrently inhibit cell wall synthesis and protein production, which are two of the five major cellular processes targeted by antibiotics, as referred to in Section 1.1. Additionally, mammals, including humans, lack the machinery to biosynthesise lysine that must be supplied through dietary intake (Dogovski *et al*, 2009; Hutton *et al*, 2007). This means that treatments focusing on the inhibition of DAPEP could potentially be selectively toxic to bacteria, whilst having no effect on mammals (Hutton *et al*, 2007).

1.5   DAPEP

DAPEP is the product of the *dapF* gene and a member of the pyridoxal phosphate-independent racemase family. This enzyme catalyses the stereochemical inversion of L,L-DAP to *meso*DAP – a critical step in the pathway because the next enzyme, DAPDC, only recognises the *meso* isomer of DAP (Sagong & Kim, 2017). Moreover, since the enzyme was first purified from *Bacillus megaterium* in 1969 (White *et al*, 1969), its structure and function has only been investigated in a limited number of bacterial species, including *E. coli, Acinetobacter baumannii, Corynebacterium glutamicum, Haemophilus influenzae* and *Mycobacterium tuberculosis* (Hor *et al*, 2013; Park *et al*, 2013; Sagong & Kim, 2017; Usha *et al*, 2008; Lloyd

et al, 2004). Accordingly, the structure and function of DAPEP from *P. aeruginosa* are yet to be elucidated.

1.5.1 Structure

While the structure of DAPEP in *P. aeruginosa* is uncharacterised, structural studies of its orthologues from *E. coli, H. influenzae* and *C. glutamicum* have revealed two homologous N- and C-terminal domains, each containing a set of eight antiparallel β-sheets, two α-helices and one catalytically important cysteine residue (Figure 3A-B) (Hor *et al*, 2013; Lloyd *et al*, 2004; Sagong & Kim, 2017). This conformation is known as the 'DAP epimerase-like' fold and is conserved across several racemase and isomerase classed proteins (Buschiazzo *et al*, 2006; Garvey *et al*, 2007; Parsons *et al*, 2004; Velarde *et al*, 2009; Blankenfeldt *et al*, 2004; Grassick *et al*, 2004; Liger *et al*, 2005). The catalytic cysteine residues found within each domain are located in the active site, where they form an interdomain disulfide bond (Figure 3A) (Hutton *et al*, 2007; Sagong & Kim, 2017). However, non-disulfide bonded conformations of DAPEP have been observed (Hor *et al*, 2013). In fact, these 'open' conformations are considered to be the biologically relevant conformations for catalytic activity, whereas those with the disulfide bridge present are inactive conformations (Cirilli *et al*, 1998; Hor *et al*, 2013; Usha *et al*, 2009). Interestingly, dimerisation of DAPEP, which is observed both in solution and crystalline states, has been shown to be essential for its function by site-directed mutagenesis (Figure 3B) (Hor *et al*, 2013). Dimerisation of the protein occurs through contacts between β-sheets on each of the monomers and between the loop of amino acids that connects the first α-helix and the third β-sheet of each monomer (Figure 3) (Sagong & Kim, 2017). Primary sequence similarity of DAPEP from *P. aeruginosa* compared to those with solved structures is variable – sharing the highest sequence identity with the *E. coli* orthologue at 56% (Madeira *et al*, 2019). Therefore, while some conserved regions of *P. aeruginosa* DAPEP could be modelled from its

orthologues, conclusive structural characterisation would require investigation of the protein directly from *P. aeruginosa*.

A

C-terminal domain   N-terminal domain

B

C

L,L-DAP   →(DAPEP)→   *meso*-DAP
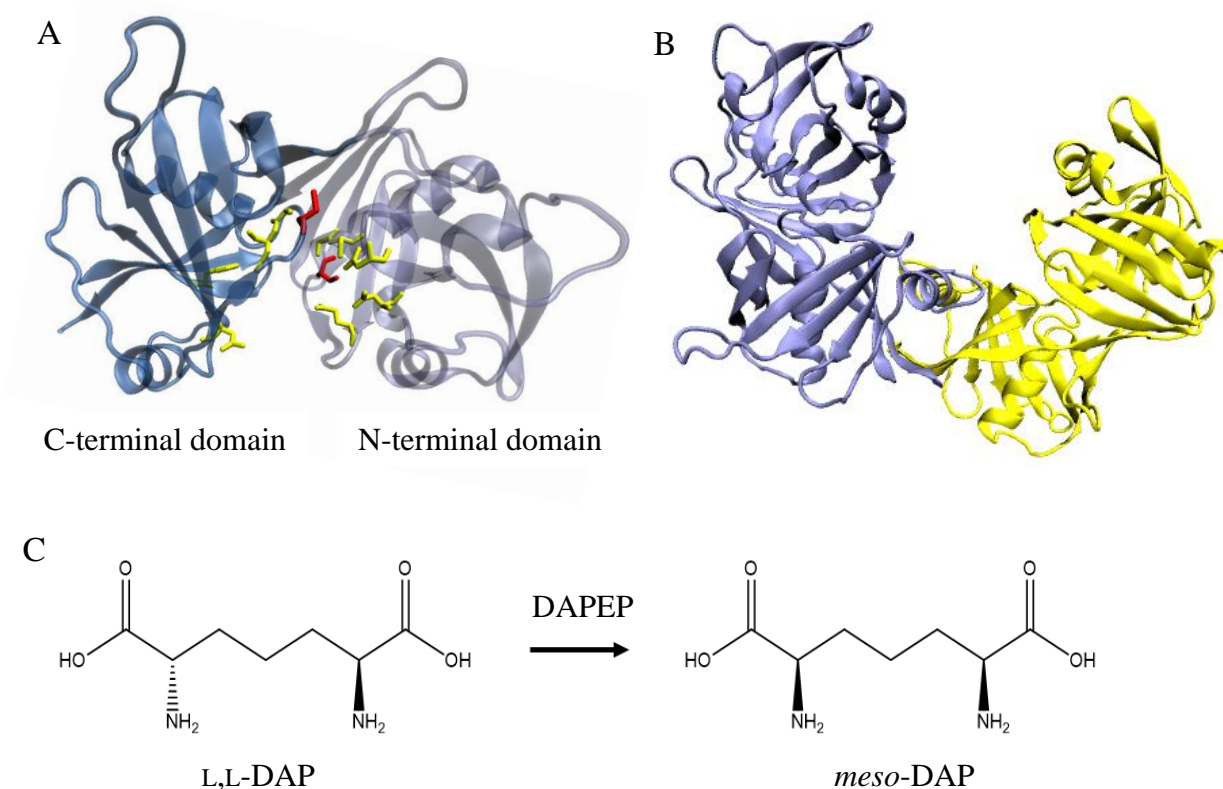
Figure 3. DAPEP structural features and catalysed reaction. (A) A magnified view of a single DAPEP monomer, which shows the active site residues in yellow and highlights the two catalytically important cysteine residues found within the N- and C-terminal domains in red. Image generated using VMD. Adapted from Hor *et al*. (2013). **(B)** The dimeric structure of the active protein with the two monomeric subunits highlighted in blue and yellow. Image generated using VMD. **(C)** In the DAPEP-catalysed reaction, the amide in L,L-DAP is repositioned around its chiral centre to form *meso*-DAP.

1.5.2   Catalytic Mechanism

As mentioned in Section 1.5, DAPEP is responsible for catalysing the interconversion of L,L-DAP to *meso*-DAP, a precursor of lysine (Sagong & Kim, 2017). Binding of the substrate to DAPEP results in a large conformational change, bringing the N- and C-terminal domains together to 'close' the enzyme and begin the interconversion (Hor *et al*, 2013). Interestingly, this interconversion requires no cofactors and functions through a two-base mechanism,

whereby two catalytically relevant cysteines act as an acid-base pair to facilitate epimerisation of the substrate (Hutton *et al*, 2007). One cysteine thiolate acts as a general base, and subsequently deprotonates the α-carbon of L,L-DAP, while the other cysteine thiol acts as a general acid to re-protonate the α-carbon from the opposite side, inverting the configuration to form *meso*-DAP (Figure 3C) (Hutton *et al*, 2007; Sagong & Kim, 2017). Interestingly, investigation into the catalytic turnover (k_{cat}) and substrate binding affinities (K_M) of DAPEP from a range of bacteria has yielded varying results. For example, in *H. influenzae*, the k_{cat} and K_M values were determined to be 128 ± 3 s^{-1} and 0.7 ± 0.1 mM, respectively, while in *C. glutamicum*, the kinetic parameters were measured at 58 s^{-1} and 1.86 mM, respectively (Koo & Blanchard, 1999; Sagong & Kim, 2017). Accurately determining these kinetic parameters for *P. aeruginosa* DAPEP is important to assess the potency of future inhibitors *in vitro*.

1.6   Assessing *meso*-DAP Depletion

As discussed in Section 1.4, the importance of *meso*-DAP on bacterial viability has not been directly characterised in the literature. Thus, tools that can achieve this outcome chemically and genetically must be established. A direct deletion of the gene encoding DAPEP in *P. aeruginosa* would be an ideal means of achieving such an outcome, as it would prevent the production of *meso*-DAP, the phenotype of which could subsequently be characterised. However, the most effective means of generating direct-gene deletions in bacteria – the lambda red recombinase system – is only available in *E. coli* and closely related species (Datsenko & Wanner, 2000). As such, alternative routes must be taken to perform gene deletions in other clinically relevant bacteria, like *P. aeruginosa*. An approach optimised by Huang and Wilks (2017), which relies on the incorporation of suicide vectors and allelic exchange, has presented itself as an efficient tool to perform accurate targeted deletions in *P. aeruginosa*. This makes it a promising means of generating deletion mutants to determine the effect of *meso*-DAP

depletion on bacterial viability. Additionally, chemical tools that inactivate *P. aeruginosa* DAPEP (PaDAPEP) could also assist with the characterisation of *meso*-DAP depletion by perturbing its production. There are only a limited number of DAPEP inhibitors, none of which have reported antibacterial activity (Pillai *et al*, 2007; Usha *et al*, 2008; Caplan *et al*, 2000). Furthermore, no inhibitors have been developed against PaDAPEP. Given that *meso*-DAP is an essential constituent of the GNB cell wall, having tools that can accurately assess the effect of its depletion would provide crucial information for the development of a new class of antibacterial agents that target its production.

1.7   Aims

The overarching goal of this project is to characterise DAPEP from *P. aeruginosa* and assess its potential as a target for the development of novel antibacterial drugs. This will be achieved through the following three aims:

1. Assess the importance of *meso*-DAP for *P. aeruginosa* survival and growth

2. Express, purify and functionally characterise PaDAPEP

3. Define the structure of PaDAPEP

Chapter Two

Developing New Tools to Assess *meso*-DAP Depletion

2.1 Introduction

Despite being a constituent of peptidoglycan in GNB, *meso*-DAP – the product of the DAPEP catalysed reaction – remains unexplored as an antibiotic target. Thus, within this chapter, efforts were made towards establishing a new tool to characterise the effect of *meso*-DAP depletion on bacterial viability and assess its potential as an antibiotic target. This approach focused on developing a genetic tool to characterise *meso*-DAP depletion by introducing a deletion of the gene that encodes DAPEP in *P. aeruginosa*. To achieve this, a modified protocol from Huang and Wilks (2017) encompassing the incorporation of suicide vectors and allelic exchange was utilised and optimised. A summary of the progress made towards achieving this gene deletion is detailed in Figure 4.
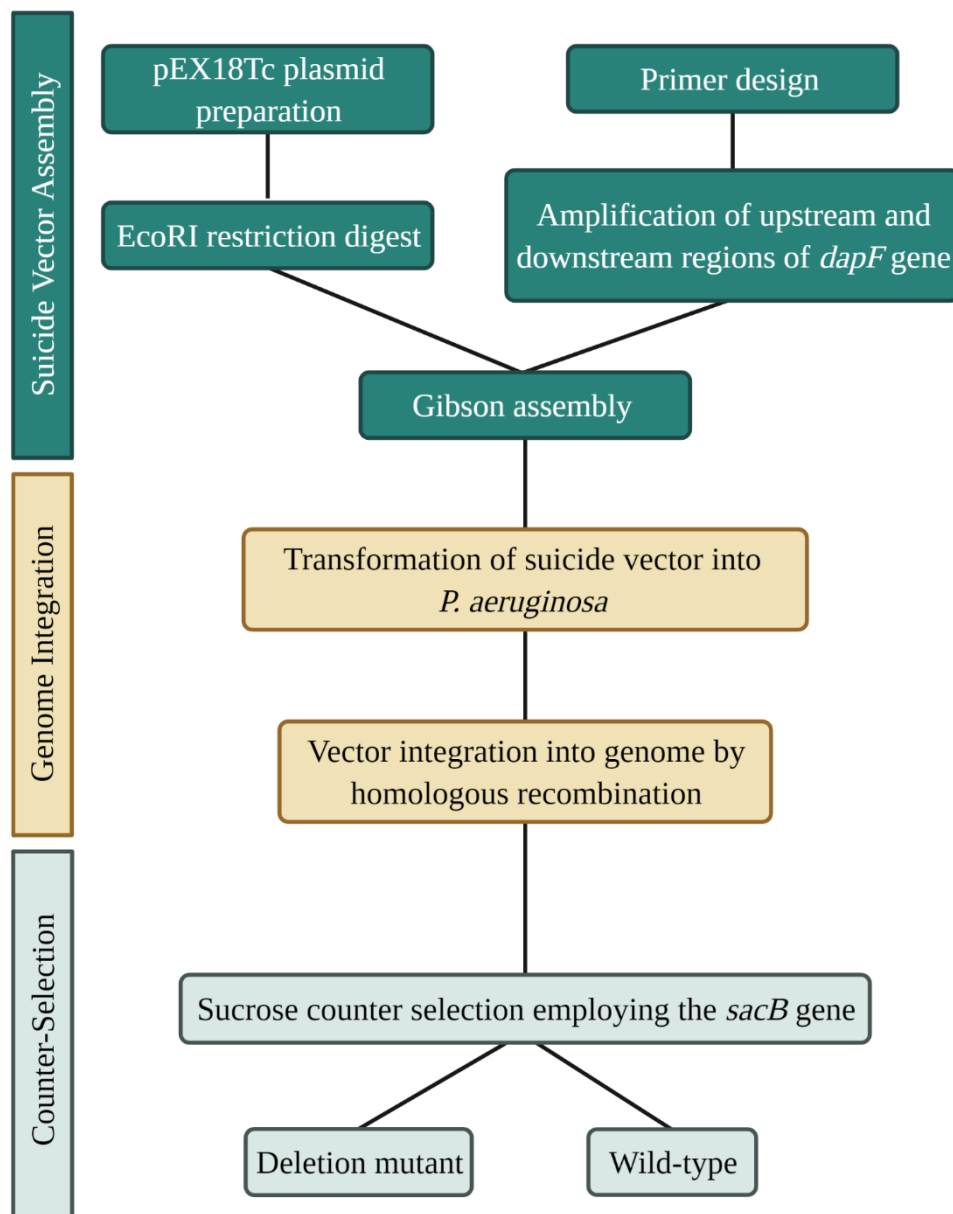
Figure 4. Flow chart summarising the steps involved in the gene knockout protocol adapted from Huang and Wilks (2017). Boxes shaded in dark green represent the completed steps in the workflow that will be described in this Chapter for introducing a deletion of the *dapF* gene in *P. aeruginosa*, while the yellow box indicates the steps being optimised. The remainder of the protocol is briefly summarised in the lighter boxes.

2.1.1 Cloning of the *dapF* Deletion Construct

Firstly, a suicide vector using the pEX18Tc plasmid containing a sequence complementary to regions flanking the *dapF* gene was designed and cloned. Initially, an EcoRI restriction digest of the pEX18Tc plasmid was performed to linearise the vector to allow for a Gibson assembly. Analysis of the digestion revealed a single ~6.5 kbp product (Figure 5A), a size that is consistent with the pEX18Tc plasmid (6845 bp). Undigested plasmid was also included in the analysis as a control to ensure its integrity. The next step required preparation of the 500 bp upstream and downstream DNA sequences of the *dapF* gene. These regions were amplified by colony PCR of *P. aeruginosa* PAO1 cells, using primers 1 and 2 (Table 3) for the upstream region and primers 3 and 4 (Table 3) for the downstream region. A single band of approximately 500 bp is observed for each product in Figure 5B, indicating the successful amplification of the flanking regions. Subsequently, the inserts and vector were assembled by Gibson assembly and the sequence verified by Sanger sequencing using primers 5 and 6 from Table 3. An excerpt from the sequencing results is shown in Figure 5C, which reveals the portion of the sequence where the upstream and downstream regions intersect, providing confirmation of a successful Gibson assembly. A plasmid map of the final suicide vector used in the subsequent transformations is shown in Figure 5D.
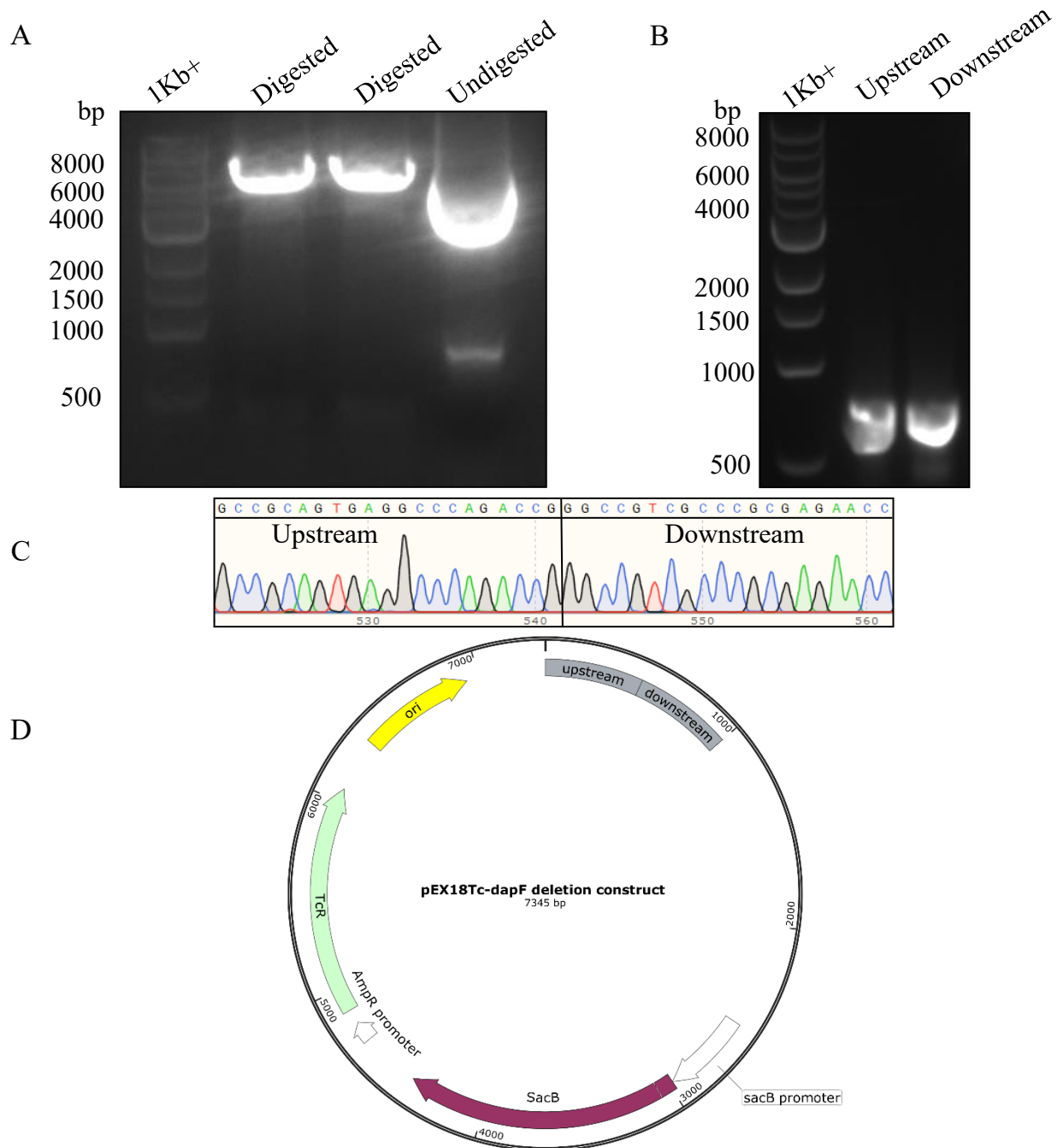
Figure 5. Assembly of the pEX18Tc-*dapF* suicide vector. **(A)** Restriction enzyme digest of pEX18Tc vector using the EcoRI restriction site. Lanes 2 and 3 contain digested plasmid showing a product at ~6.5 kbp. Lane 4 is the undigested pEX18Tc vector. **(B)** 1Taq colony PCR amplification of 500 bp upstream and downstream regions of the *dapF* gene. The PCR products were run on a 1% (w/v) agarose gel, with lanes 2 and 3 containing a single band at ~500 bp. This is consistent with the size of the 500 bp upstream and downstream regions of the *dapF* gene. **(C)** Sanger sequencing of the plasmid, highlighting the sequence where the upstream and downstream intersect, confirming the correct assembly and orientation of the inserts within the vector. **(D)** Vector map of the pEX18Tc-*dapF* suicide vector containing the homologous upstream and downstream regions of the *dapF* gene cloned within the EcoRI restriction site. Also depicted in the map is the tetracycline resistance gene (TcR), levansucrase counter selection gene (*sacB*), promoters for both selection markers (AmpR promoter and *sacB* promoter, respectively) and the origin of replication (ori).

2.1.2 Transformation of the Suicide Vector

Three methods were utilised to facilitate transformation of the suicide vector into *P. aeruginosa*: electroporation, conjugation, and heat-shock (Figure 6).
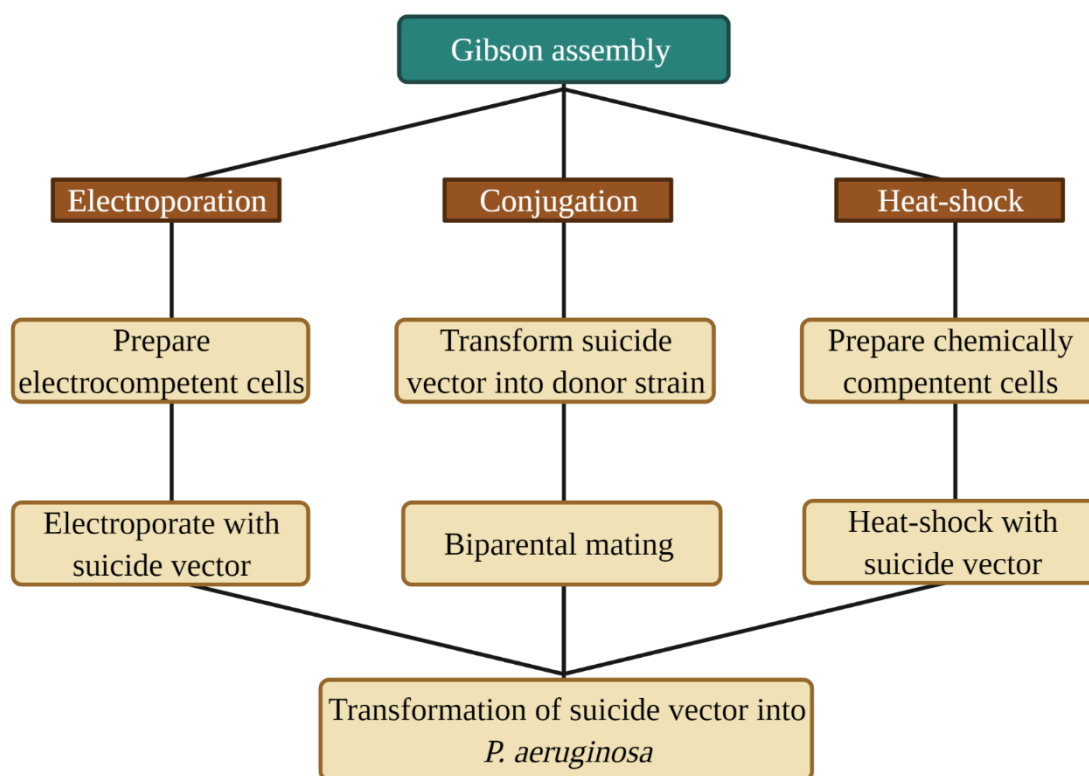
Figure 6. Flow chart of the three transformation methods employed: electroporation, conjugation, and heat-shock. The flow chart is a brief summary of the major steps involved in each of these approaches to allow for the transformation of the suicide vector into *P. aeruginosa*.

The most frequently employed transformation method, and the one used in the canonical study was electroporation. Initially, transformation of the suicide vector into *P. aeruginosa* PAO1, using the conditions from Huang and Wilks' protocol (2.2 kV, 15 ms and 600 Ω, Condition 6 [Table 1]), resulted in visible cell lysis. As such, a further 10 electroporation conditions were tested by varying the voltage and resistance (Table 1). These parameters were adjusted to

achieve pulse times closer to 5.0 ms, which has previously shown efficacy in *Pseudomonas spp.* (Iwasaki *et al*, 1994; Shen *et al*, 2006).

Table 1. Summary of electroporation conditions for transformation attempts.

Condition	Voltage (kV)	Resistance (Ω)	Pulse time (ms)	Attempts
1	2.5	200	5.0	10
2	3.0	150	3.7	8
3	1.6	200	5.0	7
4	2.0	200	5.0	4
5	3.0	200	5.0	2
6	2.2	600	15.0	1
7	1.6	250	6.3	1
8	1.6	300	7.5	1
9	1.6	400	10	1
10	1.7	200	5.0	1
11	1.9	200	5.0	1

In several of these attempts, bacterial colonies grew within the 72-hour cut off period that is stipulated by Huang and Wilks (2017). Accordingly, a colony PCR screen was completed to determine if the plasmid had been successfully integrated into the genome. The reaction employed primers 7 and 12 from Table 3 – which are complementary to the suicide vector and the PAO1 genome, respectively. Successful integration of the plasmid into the genome would result in a ~1.0 or ~1.5 kbp PCR product, while there would be no visible product in an unsuccessful integration. Analysis of the PCR products by agarose gel electrophoresis revealed no bands in each of the attempts (Figure 7). This suggests the growth of these colonies was the

result of naturally developed resistance to tetracycline, rather than conferred resistance due to integration of the suicide vector. Given the nature of the primers, no positive control could be utilised to confirm the results from the colony PCR screen. Such a control would require cloning of another vector containing regions even further upstream or downstream of the 500 bp flanking regions, which are complementary to the primers to generate a PCR product. To bypass this, the subsequent counter-selection step was completed on each of the bacterial colonies that grew within the 72-hour cut off period. Bacterial lawns were observed on the counter-selection plates, indicating no selectivity, and thus no integration of the plasmid. In additional attempts, growth of bacteria following a transformation was also supplemented with 500 µM lysine on Luria-Bertani (LB) agar plates. This was completed to counteract the possibility that integration of the plasmid into the *P. aeruginosa* PAO1 genome may have been disrupting translation of the final gene in the DAP pathway, due its proximity to *dapF*. However, this also did not result in successful integration of the plasmid. Finally, attempts to transform the suicide vector by electroporation into the *P. aeruginosa* PA14 strain were made but no colonies were observed.
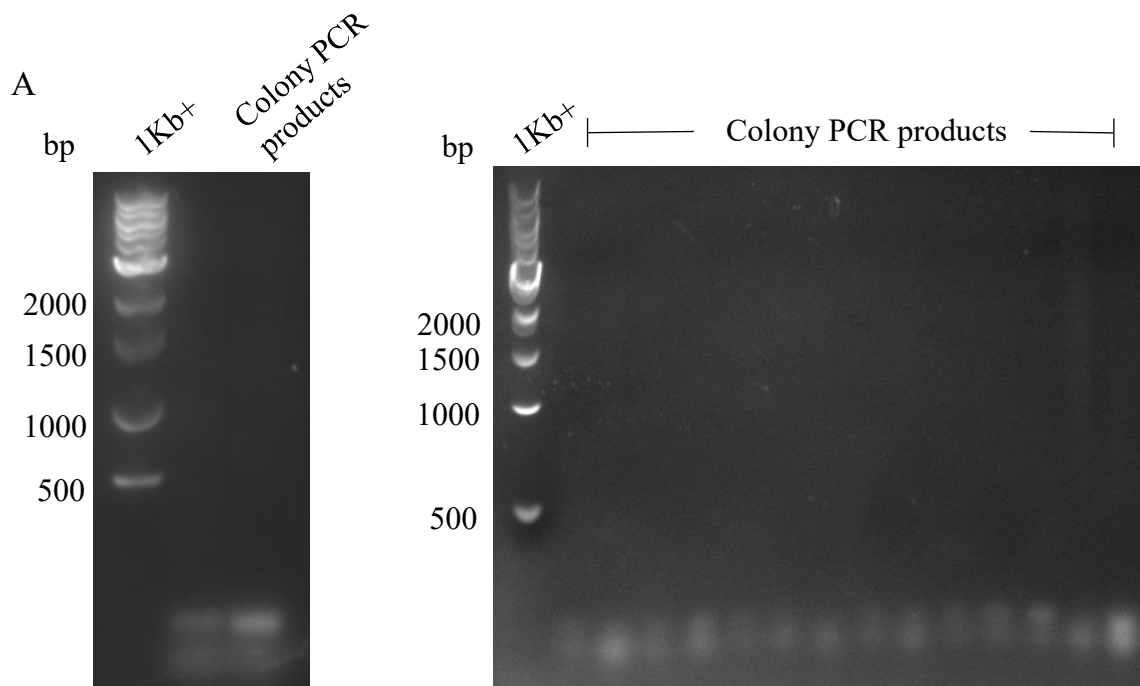
Figure 7. Integration screening following electroporation. 1Taq colony PCR to screen for integration of the suicide vector into the *P. aeruginosa* PAO1 genome. Successful integration would have yielded a ~1.0 or ~1.5 kbp product. However, no product was observed indicating that integration of the vector did not occur. The PCR products were run on a 1% (w/v) agarose gel, with all lanes, other than the DNA ladder, containing the resulting products from individual colony screening.

The second transformation method utilised a modified conjugation protocol, which relied on an *E. coli* donor strain to transform the suicide vector into *P. aeruginosa* PAO1 (Hmelo *et al*, 2015; Aparicio *et al*, 2019). To achieve this, *E. coli* S17.1 were successfully transformed with the suicide vector by electroporation. The modified *E. coli* S17.1 were then used in biparental mating with *P. aeruginosa* PAO1 to facilitate transformation of the suicide vector from the donor strain into the *P. aeruginosa* PAO1 genome. Unfortunately, completion of the protocol yielded no colonies within the 72-hour cut off period, indicating there was no integration of suicide plasmid into the genome.

The final transformation method employed to introduce the suicide vector into *P. aeruginosa* PAO1 was heat shock. This protocol adopts the use of selected transformation salts, namely $CaCl_2$ and $MgCl_2$, to make the bacterial cells chemically competent. Cells were subsequently

heat shocked with the suicide vector to transform it into *P. aeruginosa* PAO1. Yet again, several colonies appeared within the cut-off period, however, using the screening process outlined above confirmed that integration of the vector was not achieved (Figure 8).
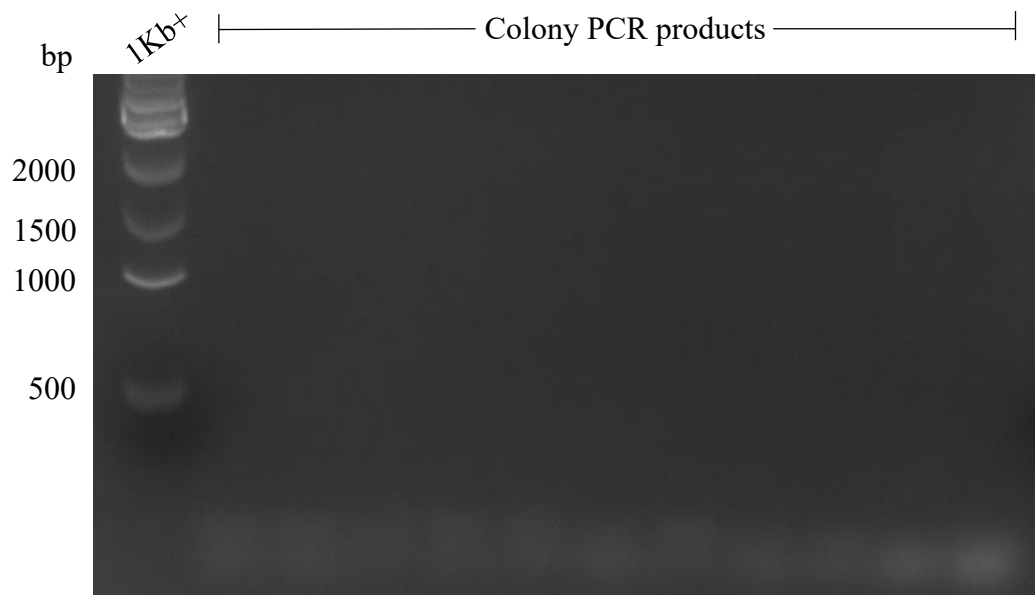
Figure 8. Integration screening following heat shock. 1Taq colony PCR to screen for integration of the suicide vector into the *P. aeruginosa* PAO1 genome following a heat shock transformation. No products were observed, indicating that integration of the vector did not occur. The PCR products were run on a 1% (w/v) agarose gel, with all lanes, other than the DNA ladder, containing the resulting products from individual colony screening.

2.2   Summary

Upstream and downstream regions of the *dapF* gene were amplified and ligated into a pEX18Tc vector via Gibson assembly. Significant optimisation and troubleshooting were performed to transform the suicide vector into *P. aeruginosa*, however, no deletion mutant was achieved. Initial steps in the protocols of three different transformation techniques were established for future attempts at generating a *dapF* gene deletion, to assess the effect of *meso-*DAP deficiency on bacterial survival and growth.

Chapter Three

Purification and Functional Characterisation

of PaDAPEP

3.1   Introduction

To assist future testing of PaDAPEP inhibitors, the enzyme must first be recombinantly produced to high purity and its kinetic activity characterised. Production of recombinant PaDAPEP to >95% homogeneity was achieved by expression in *E. coli* BL21 (DE3), followed by purification using immobilised metal affinity chromatography (IMAC). Here, the well-established DAPEP-DAPDH coupled assay was used to quantify the kinetic parameters of PaDAPEP. To achieve this, it was necessary to express and purify recombinant DAPDH from *C. glutamicum*. Subsequently, kinetic data were analysed using the Michaelis Menten model to determine the enzyme's binding affinity for its substrate (K_M), its maximal velocity upon substrate saturation (V_{max}) and its catalytic turnover number (k_{cat}).

3.2 Expression and Purification of PaDAPEP

3.2.1 Cloning of the PaDAPEP Expression Vector

To allow for the production of recombinant PaDAPEP protein, the *dapF* gene was amplified

from *P. aeruginosa* PAO1 genomic DNA by PCR employing primers 7 and 8 from Table 3.

These primers were designed with the appropriate restriction sites, either BamHI or HindIII.

Analysis of the product indicated a single band with an apparent size of ~850 bp (Figure 9A).

This is consistent with the theoretical product size, which includes the *dapF* gene, restriction

sites and flanking regions of DNA – totalling 847 bp. Subsequently, a pET28a plasmid was

prepared for insertion of the *dapF* gene by conducting a double restriction digest at the BamHI

and HindIII restriction sites. The results from the double digest revealed a single product at

approximately 5.5 kbp in length (Figure 9B), which is consistent with the size of the pET28a

plasmid (5369 bp). The analysis also included undigested pET28a plasmid as a control to

confirm its linearisation (Figure 9B). Finally, the *dapF* gene was ligated into the BamHI and

HindIII digested pET28a vector using T4 DNA ligase, resulting in the protein expression vector

depicted in Figure 9C. The plasmid was subjected to Sanger sequencing using primers 9 and

10 (Table 3). The results confirmed successful ligation of the insert and ensured no mutations

were introduced into the *dapF* gene during PCR.
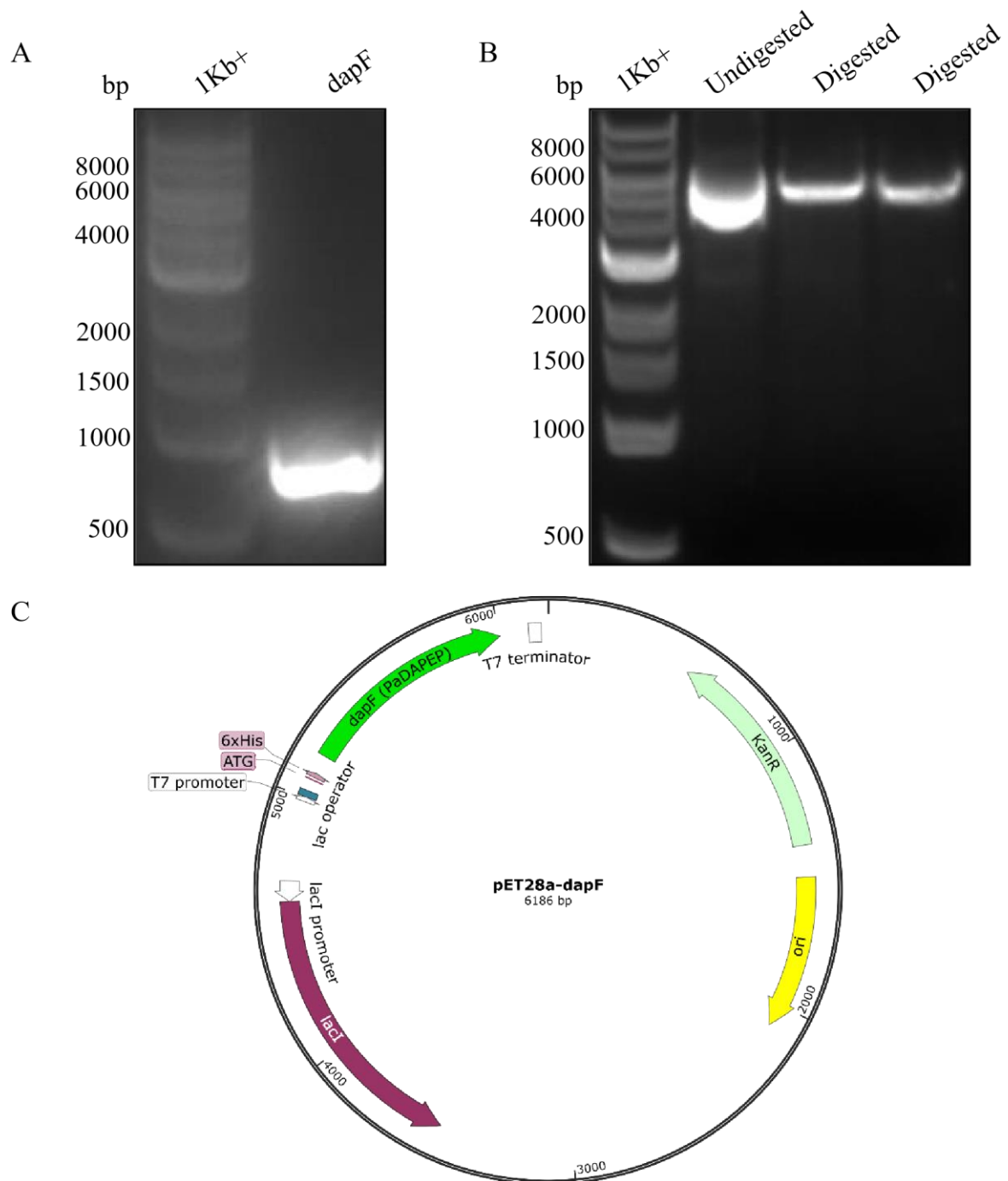
Figure 9. Cloning of the pET28a-*dapF* expression vector. (**A**) Phusion PCR amplification of the *dapF* gene. The PCR product was run on a 1% (w/v) agarose gel. In lane 2, a band can be observed at ∼800 bp that is representative of the *dapF* gene from *P. aeruginosa*. (**B**) Restriction enzyme digest of pET28a vector using BamHI and HindIII restriction enzymes. The products of the digestion were run on a 1% (w/v) agarose gel. Lane 2 is the undigested pET28a vector. Lanes 3 and 4 contain digested plasmid with a predicted product between 5000 and 6000 bp. (**C**) pET28a vector map with the *dapF* insert cloned utilising the BamHI and HindIII restriction sites. Also depicted in the map is the kanamycin resistance gene (KanR), lac operon (lacI), lacI promoter, origin of replication (ori), purification tag (6× His), T7 promoter and terminator.

3.2.2 Optimisation of PaDAPEP Expression Conditions

Following the successful cloning of the pET28a-*dapF* plasmid, small-scale expression trials were completed to elucidate the optimum temperature conditions for protein overexpression in *E. coli* BL21 (DE3) cells. Overexpression was assessed by sodium dodecyl sulphate-polyacrylamide gel electrophoresis (SDS-PAGE) analysis of the soluble and insoluble crude cell lysate fractions incubated at 16, 25 or 37 °C after isopropyl-β-D-thiogalactoside (IPTG) induction. At 16 and 25 °C, overexpression of a single protein with an apparent mass of ~33 kDa was observed (Figure 10), which is comparable to the expected theoretical mass of recombinant PaDAPEP ($M_r = 33638.7$ Da). While both temperatures resulted in overexpression of the protein, there was a slightly higher protein yield at 16 °C, and thus, this was the chosen condition for large-scale expression. Importantly, the protein appears in the soluble fraction (Figure 10), suggesting no further optimisation of the expression conditions was required for large-scale protein expression.
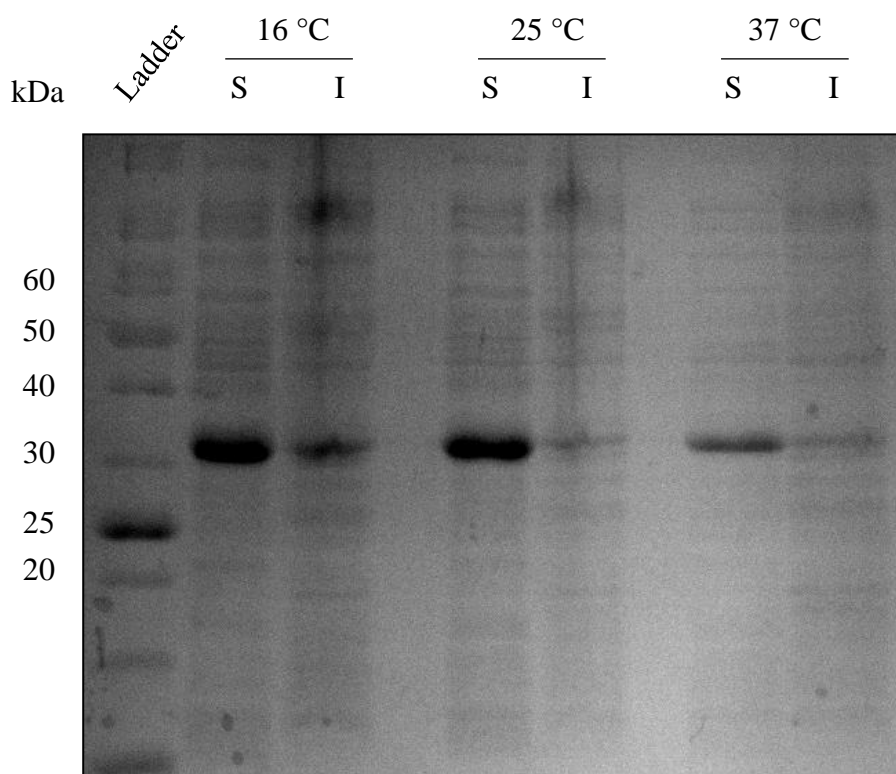
Figure 10. Protein expression temperature optimisation trials for PaDAPEP. Expression of PaDAPEP was assessed at 16, 25 and 37 °C. Samples were analysed by SDS-PAGE on a 12% (w/v) polyacrylamide gel using the NEB Broad Range Unstained Protein Standard for size estimation. Lanes contain either soluble (S) or insoluble (I) fractions of lysed *E. coli* BL21 (DE3) cells incubated at 16, 25 or 37 °C following IPTG induction. A single overexpression band in each of the soluble fractions is visible at approximately 33 kDa, which is equivalent to the theoretical mass of recombinant PaDAPEP (M_r = 33639 Da).

3.2.3 Large-Scale Protein Expression and Purification

Using the optimised overexpression conditions from the previous section, an up-scaled overexpression experiment to produce recombinant PaDAPEP was conducted using 2 L of bacterial culture. Following overexpression, the protein was purified by IMAC, as detailed in Section 6.2.3.7. Elution of PaDAPEP occurred from 240 – 290 mM imidazole (Figure 11A). Fractions were analysed by SDS-PAGE and those with >95% PaDAPEP purity were pooled and dialysed into Buffer C (Table 8). This resulted in a yield of 30 mg of PaDAPEP per litre of expression culture. A summary of the purification steps can be seen in Figure 11B.

The expression and purification of DAPDH from *C. glutamicum* (CgDAPDH) was also completed as it is the coupling enzyme required for the PaDAPEP kinetic assay. The incubation was completed at 25 °C, using conditions that have been shown to result in overexpression of the enzyme (Mackie, unpublished). Purification of CgDAPDH (M_r = 37689 Da) was also achieved by IMAC, with elution of the protein at approximately 100 – 150 mM imidazole (Figure 11C). Elution fractions were subsequently assessed for purity by SDS-PAGE and fractions with >95% purity were pooled and dialysed into Buffer C (Table 9). This resulted in a yield of 23 mg of CgDAPDH per litre of expression culture. The purification steps are summarised in Figure 11D.
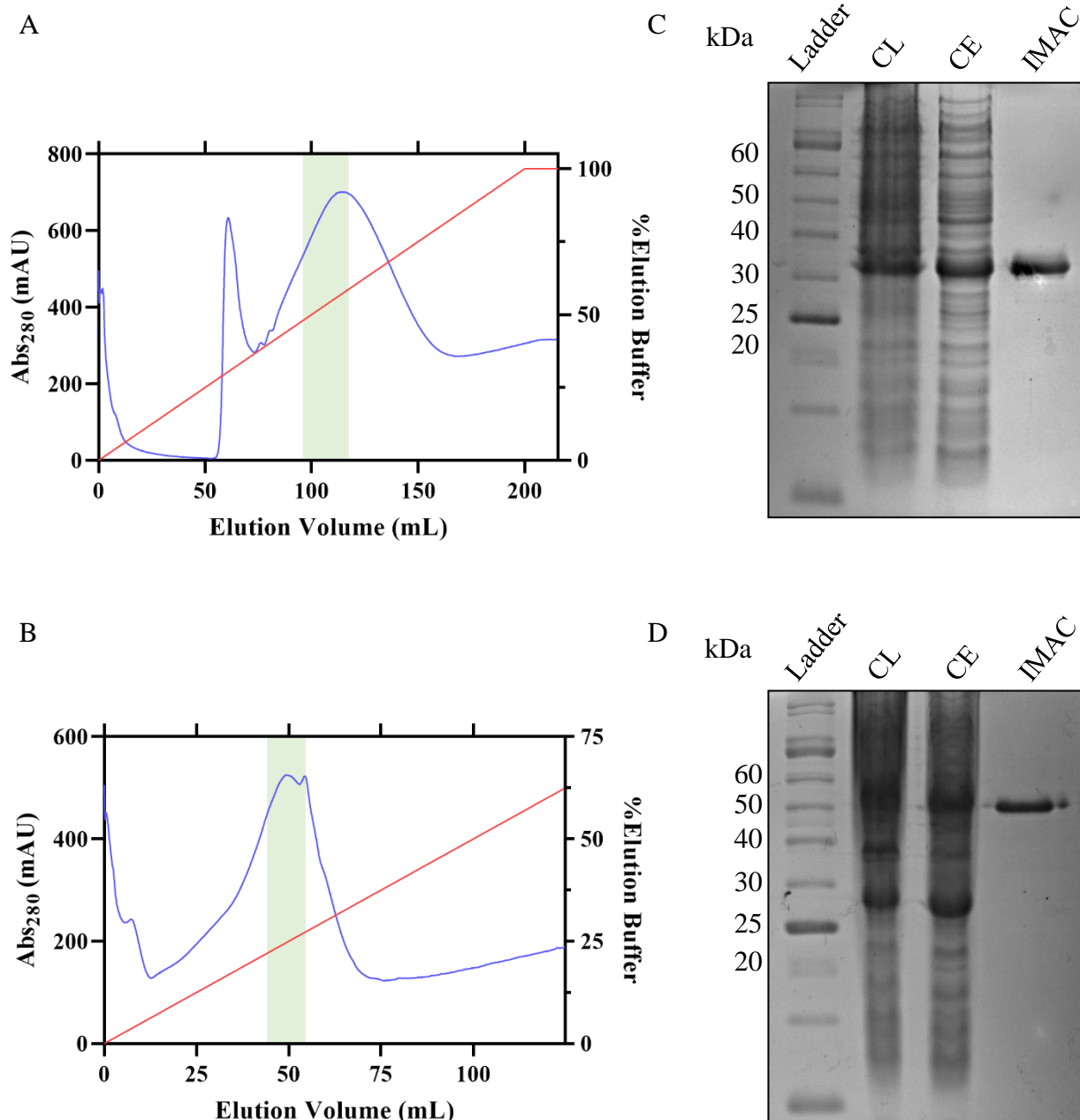
Figure 11. Purification of recombinant PaDAPEP and CgDAPDH. Chromatograms detailing the IMAC purification of (**A**) PaDAPEP and (**B**) CgDAPDH with absorbance at 280 nm and % elution buffer (red line) plotted as a function of elution volume. Elution fractions were analysed by SDS-PAGE and those containing PaDAPEP and CgDAPDH (green shading) at >95% purity were subsequently pooled. Summary gels for the purification of (**C**) PaDAPEP and (**D**) CgDAPDH showing the purification of the protein from the crude lysate (CL) to crude extract (CE) and the final IMAC purification. Size was estimated using the NEB Broad Range Unstained Protein Standard.

3.3   Catalytic Parameters of PaDAPEP

3.3.1   Initial Rate Analysis of the PaDAPEP Catalysed Reaction

Prior to the kinetic characterisation of PaDAPEP, it was necessary to ensure that the recombinant enzyme was functional and that a suitable concentration was determined for subsequent kinetic assays. To do so, the DAPEP-DAPDH coupled assay was used to measure the initial rate of the reaction at PaDAPEP concentrations between $0 - 400$ nM. Briefly, following the epimerisation of L,L-DAP to *meso*-DAP by DAPEP, *meso*-DAP is converted to tetrahydrodipicolinate by DAPDH – a reaction that reduces $NADP^+$ to NADPH. The coupled assay works by measuring the change in absorbance at 340 nm as a result of the reduction of the cofactor $NADP^+$. The assay was conducted in technical triplicate, indicating a linear relationship between the reaction rate and the amount of available DAPEP within the reaction (Figure 12). A PaDAPEP concentration of 63 nM was chosen for subsequent catalytic parameter characterisation as it ensures a measurable rate.
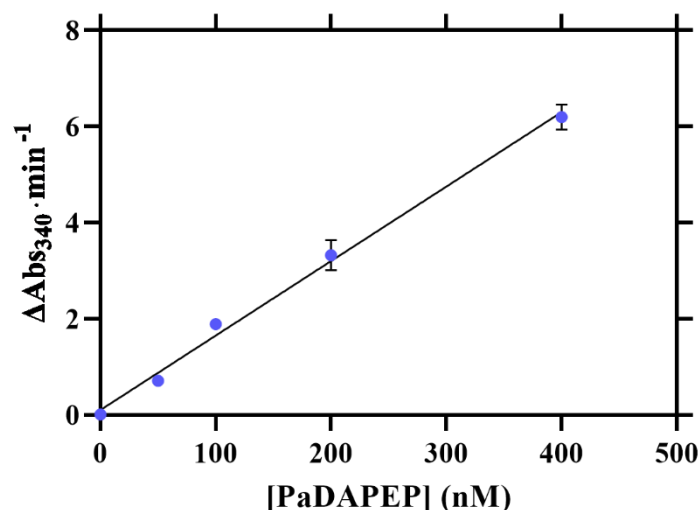
Figure 12. Initial rate analysis of the PaDAPEP catalysed reaction at different enzyme concentrations. Initial rate data were plotted as a function of PaDAPEP concentration. Data were collected in technical triplicate and fitted to a linear regression model with an R^2 value of 0.99. Error bars represent S.D. (n = 3).

3.3.2 Michaelis-Menten Analysis

The catalytic parameters of PaDAPEP were determined from one experiment in technical triplicate by measuring the initial rate of the DAPEP-DAPDH coupled reaction using a fixed PaDAPEP concentration and varied concentrations of the substrate, L,L-DAP. Initial rate was plotted as a function of L,L-DAP concentration (Figure 13). The resulting data were fitted to the Michaelis-Menten equation (Equation 1), yielding a K_M for L,L-DAP of 0.140 ± 0.03 mM, a V_{max} of 225 ± 13 µmol·mg^{-1}·min^{-1} and a k_{cat} of 127 ± 6 s^{-1}.
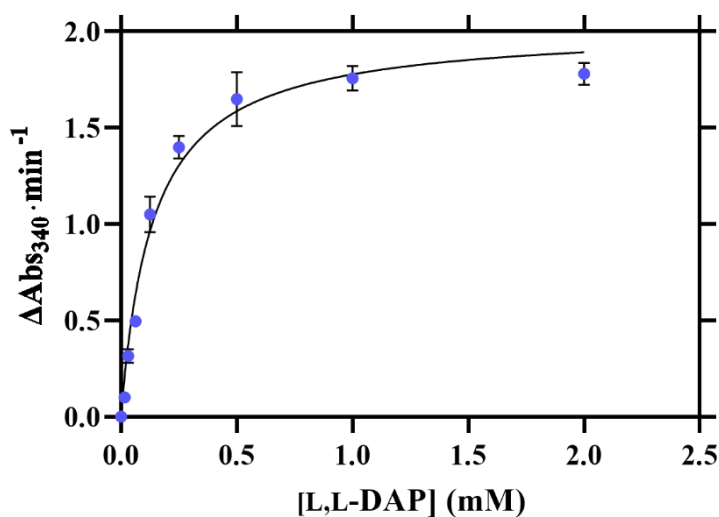
Figure 13. Michaelis-Menten analysis of recombinant PaDAPEP. Initial rate plotted as a function of L,L-DAP concentration. Data were collected in triplicate and fitted to the Michaelis-Menten equation with an R^2 value of 0.98, yielding a K_M of 0.14 ± 0.03 mM and a V_{max} of 225 ± 13 µmol·mg^{-1}·min^{-1}. Error bars represent S.D. (n = 3).

3.4 Summary

A protein expression vector for PaDAPEP was cloned from *P. aeruginosa* genomic DNA and used to recombinantly synthesise the enzyme. Expression conditions were found to be optimum at 16 °C and the recombinant enzyme was subsequently purified to >95% homogeneity. Steady-state kinetics were employed to determine the catalytic parameters of PaDAPEP using a coupled assay. The K_M for L,L-DAP was determined to be 0.140 ± 0.03 mM, the maximal velocity of the enzyme was 237 $\mu mol \cdot mg^{-1} \cdot min^{-1}$ and the catalytic turnover was calculated to be 127 ± 6 s^{-1}. Understanding the kinetic parameters of PaDAPEP is essential for determining the *in vitro* potency of future inhibitors as they provide baseline values from which efficacy of inhibitors can be tested and compared.

Chapter Four

Structural Characterisation of PaDAPEP

4.1   Introduction

To pursue a structure-based inhibitor discovery approach for the design of PaDAPEP inhibitors, this chapter focuses on elucidating the structure of the enzyme both in solution and crystalline states. The in-solution secondary and quaternary structures were assessed using circular dichroism (CD) spectroscopy and analytical ultracentrifugation (AUC), respectively. Additionally, the 3-D structure of PaDAPEP was elucidated by X-ray crystallography, which helped to identify important structural components that could be targeted for future inhibitor discovery.

4.2 In Solution Characterisation

4.2.1 Secondary Structure

Following successful purification of PaDAPEP, the secondary structure of the protein was quantitatively analysed by CD spectroscopy. Analysis of the CD spectra, plotted as the change in extinction coefficient as a function of wavelength, predicts a single minimum peak at ~215 nm (Figure 14). This is a characteristic found predominantly in β-structure proteins and is consistent with known DAPEP structures from other bacterial species (Hor *et al*, 2013; Cirilli *et al*, 1998; Sagong & Kim, 2017; Usha *et al*, 2009). The proportion of the secondary structural elements was determined by fitting the data to the CONTINILL algorithm (RMSD = 0.074) using the SP29 data set for reference (Figure 14). The resulting structural composition was calculated to be 6% α-helical, 65% β-structure and 29% unordered.
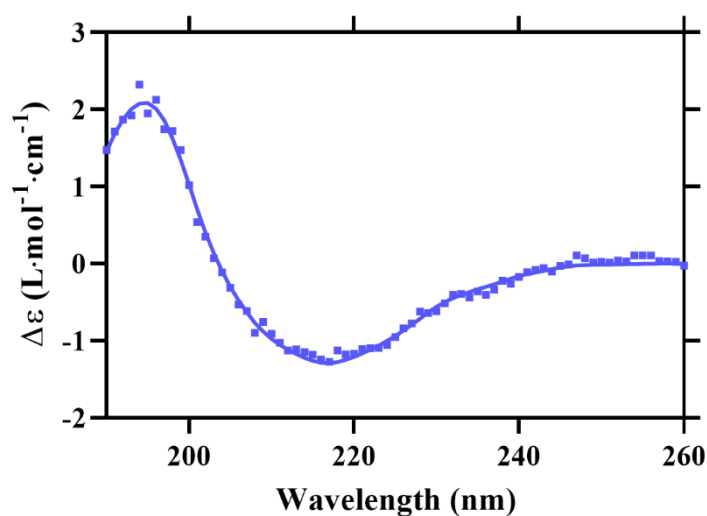
Figure 14. Circular dichroism spectra of recombinant PaDAPEP. CD spectra plotted as change in extinction coefficient versus wavelength for PaDAPEP. Experimental data were collected from 190 – 260 nm (squares) and fitted to the CONTINILL algorithm using the CDPro software, employing the SP29 data set (solid line) with an RMSD of 0.074.

4.2.2 Quaternary Structure

Having confirmed the secondary structure composition of PaDAPEP, AUC was used to determine the oligomeric state of the recombinant enzyme in solution. A sedimentation velocity experiment was conducted at final protein concentrations of 0.30 and 0.90 mg/mL. Data from the analysis were fitted to a sedimentation coefficient distribution model [$c(s)$], as seen in Figure 15. The distribution revealed a single ~4 S protein species, which corresponds to a molar mass of ~ 60 kDa. Given the theoretical mass of recombinant PaDAPEP ($M_r = 33639$ Da), the results suggest the protein exists as a dimer in solution. This further supports the hypothesis that dimerisation is essential for DAPEP catalytic activity (Hor *et al*, 2013).
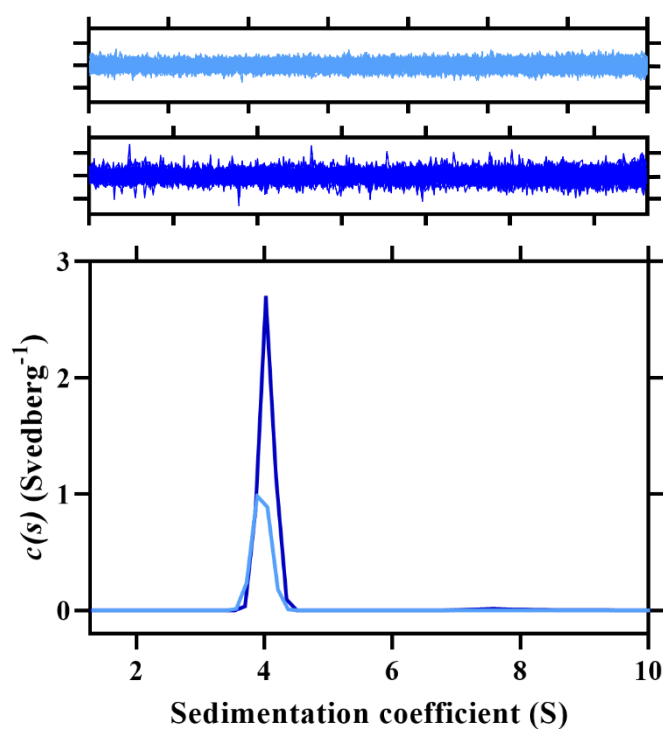
Figure 15. Sedimentation velocity analysis of PaDAPEP. Continuous size distribution *c(s)* plotted as a function of sedimentation coefficient at PaDAPEP concentrations of 0.30 mg/mL (light blue) and 0.90 mg/mL (dark blue). Residuals corresponding to the *c(s)* distribution fits are displayed above in the respective colours of each concentration.

4.3 Crystal structure

4.3.1 Crystallisation Trials

To determine the tertiary structure of PaDAPEP, crystallisation screens were conducted in collaboration with C3 (CSIRO) utilising the Shotgun screen at protein concentrations of 6.0 and 11 mg/mL. Nine initial crystallisation conditions were successfully identified at both protein concentrations (Figure 16). Subsequently, a matrix of 48 conditions optimised from the Shotgun screen were tested in-house employing the hanging drop-vapour diffusion method to produce larger crystals more suitable for X-ray diffraction (Tables 10 and 11). The optimisations included conditions with varied buffers, pH values and reagent concentrations. This resulted in a further nine conditions that facilitated nucleation and growth of PaDAPEP crystals. The most promising condition contained 11 mg/mL PaDAPEP, 24% (w/v) polyethylene glycol (PEG) 3350, 0.28 M ammonium sulfate, 0.10 M sodium MES (pH 6.4), with crystals forming between 7 and 10 days.
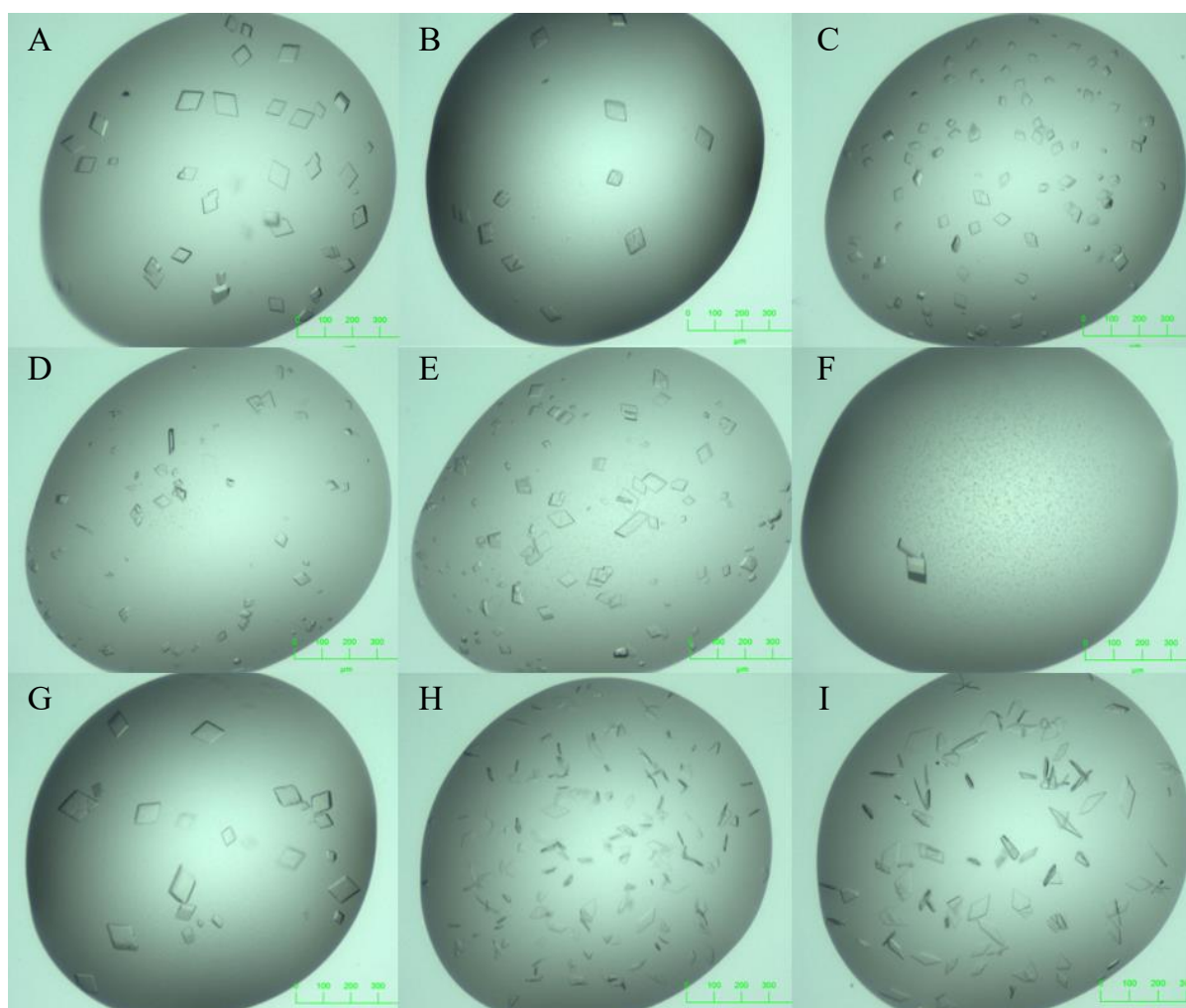
Figure 16. Initial PaDAPEP crystallisation conditions from Shotgun screen. (A) 25% (w/v) polyethylene glycol (PEG) 3350, 0.20 M sodium acetate, 0.10 M bris-tris chloride (pH 5.5) and 11 mg/mL PaDAPEP. **(B)** 25% (w/v) PEG 3350, 0.10 M bis-tris chloride (pH 5.5) and 6.0 mg/mL PaDAPEP. **(C)** 25% (w/v) PEG 3350, 0.20 M sodium acetate, 0.10 M bris-tris chloride (pH 5.5) and 6.0 mg/mL PaDAPEP. **(D)** 17% (w/v) PEG 3350, 0.10 M sodium acetate, 0.1 M bis-tris chloride (pH 5.5) and 6.0 mg/mL PaDAPEP. **(E)** 17% (w/v) PEG 3350, 0.10 M sodium acetate, 0.1 M bis-tris chloride (pH 5.5) and 11 mg/mL PaDAPEP. **(F)** 20% (w/v) PEG 8000, 0.20 M sodium acetate, 0.10 M sodium MES (pH 6) and 11 mg/mL PaDAPEP. **(G)** 25% (w/v) PEG 3350, 0.10 M bis-tris chloride (pH 5.5) and 11 mg/mL PaDAPEP. **(H)** 25% (w/v) PEG 3350, 0.20 M ammonium sulfate, 0.10 M bis-tris chloride (pH 6.5) and 6.0 mg/mL PaDAPEP. **(I)** 25% (w/v) PEG 3350, 0.20 M ammonium sulfate, 0.10 M bis-tris chloride (pH 6.5) and 11 mg/mL PaDAPEP.

4.3.2 Diffraction Data, Model Building and Refinement

Diffraction data were collected to 1.74 Å resolution from a PaDAPEP crystal on the MX2 beamline at the Australian Synchrotron. The dataset was processed using XDS (Kabsch, 2010) and scaled using AIMLESS (Evans & Murshudov, 2013) in the $P2_1$ space group (Table 2). The phase was solved using DAPEP from *Arabidopsis thaliana* (Protein Data Bank ID: 3EKM) as a search model for molecular replacement in the software pipeline AUTO-RICKSHAW (Panjikar *et al*, 2005; 2009). This yielded well-defined electron density throughout the molecule, as seen in Figure 17, allowing for iterative cycles of model building and refinement were carried out using COOT (Emsley *et al*, 2010) and PHENIX.REFINE (Afonine *et al*, 2012), respectively. Refinement parameters included a Translation/Libration/Screw (TLS) refinement using chains identified by the TLSMD online server (Painter & Merritt, 2006). The model was refined to a final R_{free} of 21%, with no Ramchandran outliers and 98% of residues within the favoured region. Finally, the quality of the structure was assessed in COOT and the online PDB validation tool (Berman *et al*, 2003; Emsley *et al*, 2010). Data from the refinement is shown in Table 2.
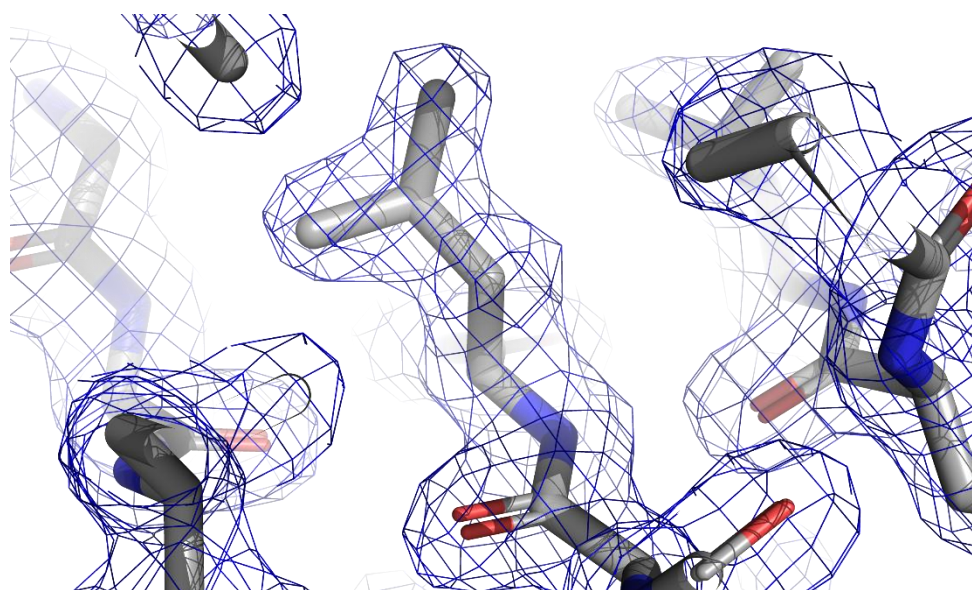
Figure 17. Leu240 and surrounding residues covered by 2*Fo-Fc* electron density map (blue). Electron density map is contoured at 1σ, demonstrating quality of electron density data.

Table 2. Data and refinement statistics for PaDAPEP crystal structure. Data collection statistics following a '/' are for the high-resolution shell.

Data collection	Value
Space group	P2$_1$
Unit-cell parameters (Å, °)	57.82, 50.89, 105.69, 90, 105.69, 90
Resolution (Å)	19.49 – 1.74
No. of observations	418288/66865
No. of unique reflections	118623/18598
Completeness (%)	98.7/96.6
Redundancy	3.53/3.60
R$_{merge}$	5.4/78.8
R$_{meas}$	6,4/92.4
CC$_{1/2}$	99.8/69.1
Average $I/\sigma(I)$	10.49/1.25
Refinement	
R (%)	18.3/32.7
R$_{free}$ (%)	21.1/33.1
No. of reflections in test set	1478
No. of protein molecules per asu	2
R.M.S.D bond length (Å)	0.012
R.M.S.D bond angle (°)	1.218
Average B-factors (Å^2)	
Protein molecules	42.45
Ligand molecules	-
Water molecules	42.34
Ramchandran plot	
Most favoured regions (%)	98.18
Additionally allowed regions (%)	1.82
Disallowed regions (%)	0.0

4.3.3   General Features

The refined PaDAPEP model reveals a dimeric enzyme made up of monomers A and B, with 272 amino acid residues each. While the recombinantly produced PaDAPEP has 311 amino acid residues, 33 N-terminal residues were revealed to form a disordered chain that could not be modelled due to lack of electron density. This region houses important elements for protein production and purification that are not found in the endogenous protein. Importantly, the remainder of each monomer was able to be modelled and adopts the 'DAP epimerase-like' fold (Section 1.5.1), a conformation that is thought to be conserved across other enzymes in the protein superfamily (Figure 17A). Found within each monomer are structurally similar N-

terminal (residues 34-155 and 302-311) and C-terminal (residues 156-301) domains, comprising of eight mixed β-sheet folds that form a barrel and two α-helices – one found within the β-barrel structure, and another on the protein's surface. These domains are pseudo-symmetrical with a root-mean-square deviation (RMSD) of 3.0 Å over 70 α-carbon pairs, while sharing only 16% sequence identity (Figure 17B). An overlay of the individual monomers suggests they are essentially identical, with the only noticeable difference being in a β-turn motif between residues 179 and 182. The alignment resulted in an RMSD of 0.11 Å over 245 α-carbon pairs (Figure 17C).
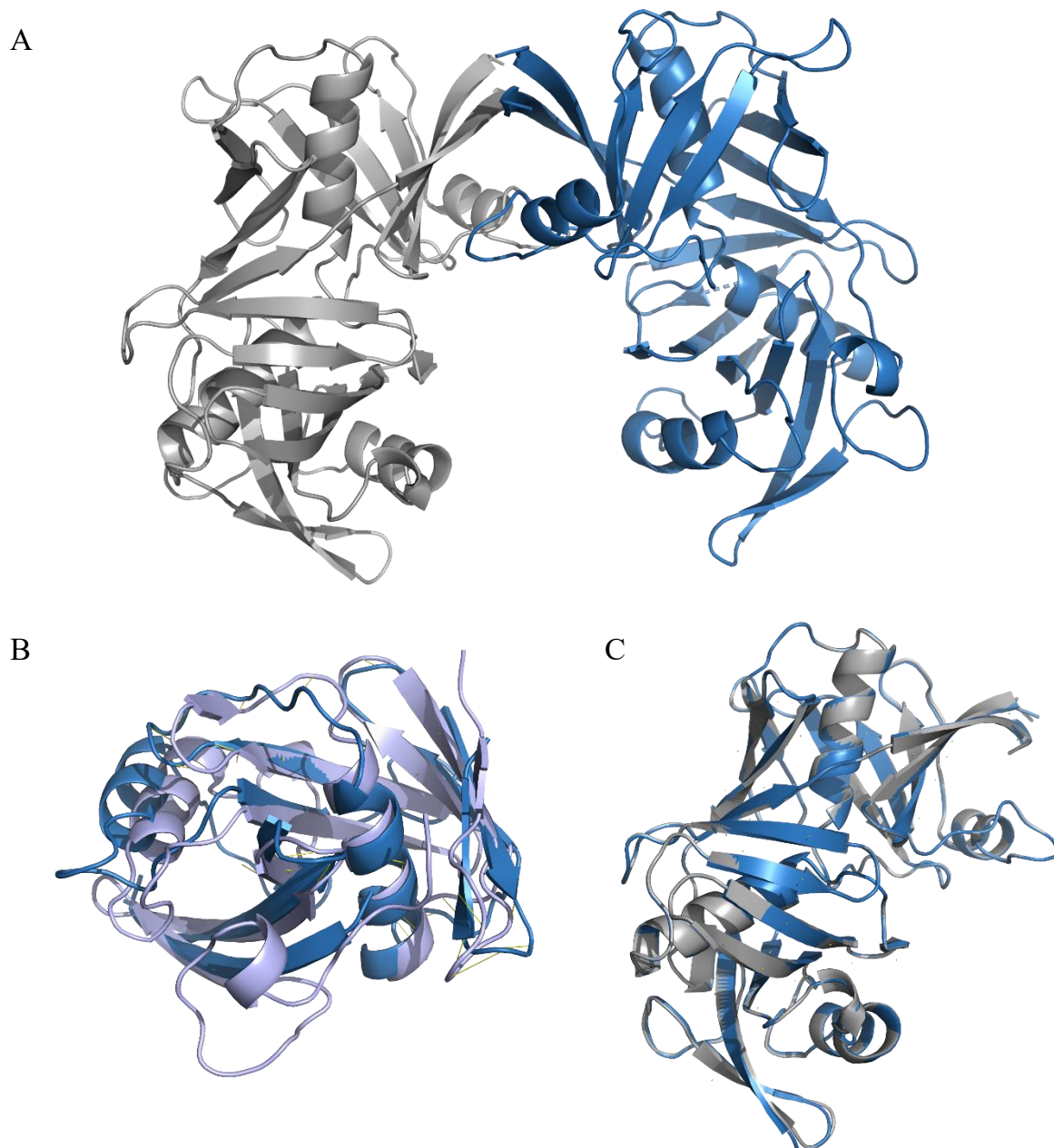
Figure 18. General tertiary structure features of PaDAPEP. (A) Refined PaDAPEP model revealing its dimeric structure and the canonical 'DAP epimerase-like fold' that each monomer adopts. **(B)** Structural alignment of the N- (blue; residues 34-155 and 302-311) and C-terminal (purple; residues 156-301) domains of PaDAPEP, which exhibit pseudo-symmetry with a rootmean-square deviation (RMSD) of 3.0 Å over 70 α-carbon pairs. **(C)** Structural alignment the A and B monomers that constitute the full dimeric structure, resulting in an RMSD of 0.11 Å. Images generated using PYMOL (version 4.6).

4.3.4 Gram-negative Fold Comparison

To assess the degree of structural conservation of DAPEP amongst Gram-negative pathogens,

the structure of PaDAPEP was overlayed with orthologues from all known GNB with a solved

crystal structure of DAPEP. PaDAPEP shared the highest degree of structural similarity with the enzyme from *H. influenzae* (1GQZ) with an RMSD of 1.5 Å. However, DAPEP in this model is monomeric, thus the alignment could only be performed across 250 α-carbon pairs (Lloyd *et al*, 2004). Alignments of the enzyme from *A. baumannii* (5HA4) and *E. coli* (4IJZ) against PaDAPEP resulted in an RMSD of 2.0 Å over 533 α-carbon pairs and 2.5 Å over 511 α-carbon pairs, respectively (Figure 18) (Hor *et al*, 2013; Mayclin *et al*, 2015). Visually, slight differences in the positioning of motifs within the enzymes can be observed, however, the tertiary structure remains largely consistent across each model.
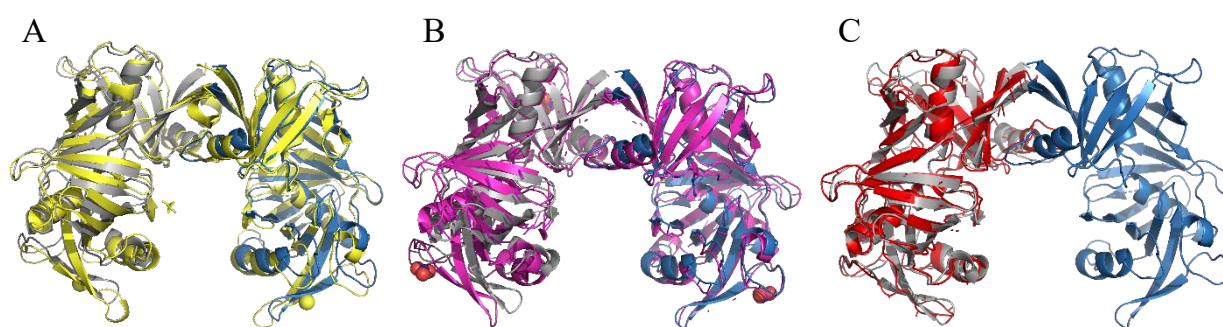
Figure 19. Structural alignments of PaDAPEP against orthologues from other GNB. (A) Alignment of PaDAPEP and *A. baumannii* DAPEP leading to a root-mean-square deviation (RMSD) of 2.0 Å (5HA4; 533 α-carbon pairs). **(B)** Alignment of PaDAPEP and *E. coli* DAPEP resulting in an RMSD of 2.5 Å (4IJZ; 511 α-carbon pairs). **(C)** Alignment of PaDAPEP and *H. influenzae* DAPEP yielding an RMSD of 1.5 Å (1GQZ; 250 α-carbon pairs). Images generated using PYMOL (version 4.6).

4.3.5   Active Site of PaDAPEP

Examination of the crystal structure of PaDAPEP shows that the active site is located in a cleft distal to the α-helix found within the β-barrel structure of each domain. The 16 conserved active site residues can be found within this cleft, including the two cysteine residues (109 and 252) responsible for catalysing the reaction, which can be seen in the oxidised form, or the 'closed' conformation (Figure 19).
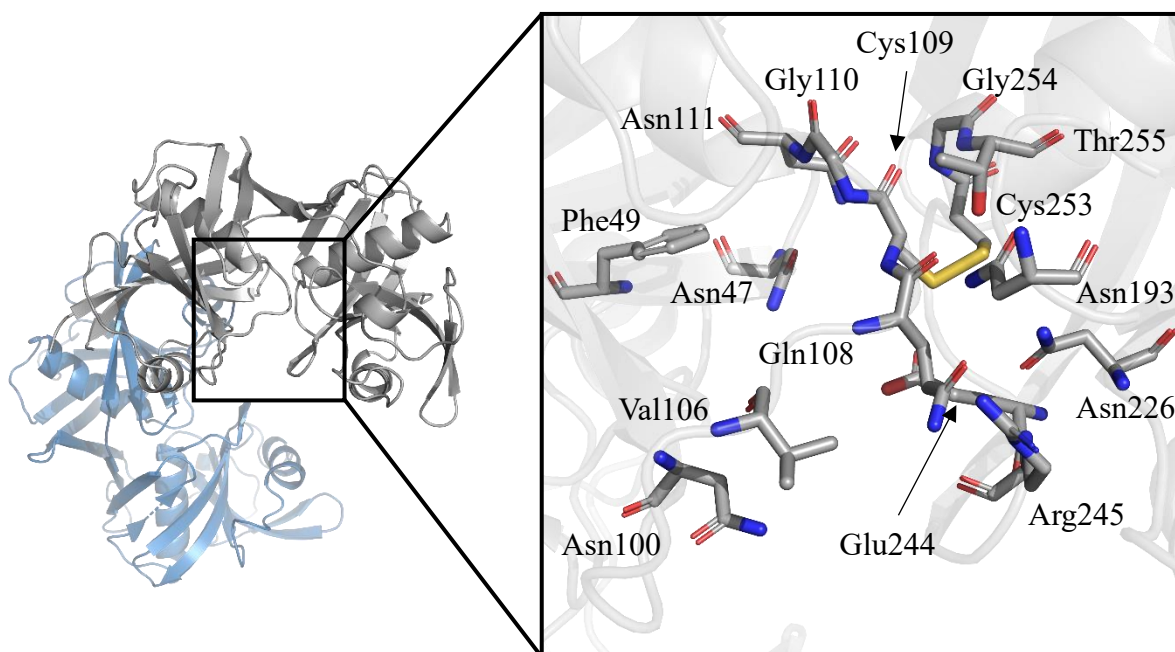
Figure 20. PaDAPEP active site residues. Magnified view of the active site residues retrieved from the PaDAPEP crystal structure. Images generated using PYMOL (version 4.6).

While this does not represent the catalytically active conformation of the enzyme, the positioning of the cysteines and the remaining active site residues can provide important insights into the differences in kinetic parameters observed between PaDAPEP and its orthologues. To assess these differences, structural alignments of the residues in PaDAPEP with respective residues from the enzyme in both *H. influenzae* (Hi) and *C. glutamicum* (Cg) were completed. DAPEP from these bacteria was similarly crystalised in the 'closed' conformation and had associated kinetics data to enable the comparison. The alignment from *H. influenzae* resulted in an RMSD of 1.5 Å over 15 α-carbon pairs (Figure 20A). Visual inspection of the analysis reveals that the active site residues and those surrounding them are generally closer to the active site cleft in PaDAPEP, where the enzyme binds L,L-DAP. For example, the α-carbon of Asn47 is 2.9 Å closer to the cleft in PaDAPEP when compared to HiDAPEP. The sidechain of Phe49, the α-carbon of Gln108 and the sidechain of Arg245 also exhibited this property, as they were 2.2, 1.7 and 2,1 Å closer to the cleft, respectively. This

positioning bias towards the active site cleft was also observed in the structural alignment with CgDAPEP – albeit to a lesser extent (Figure 20B). The alignment between CgDAPEP and PaDAPEP was conducted over 14 α-carbon pairs, resulting in an RMSD of 0.86 Å. In this analysis, while Phe49 and Asn47 were similarly positioned, the sidechains of Asn193, Arg245 and Glu244 were 3.9, 2.1 and 3.5 Å closer. Interestingly, the glutamine at position 108 is replaced with a methionine in CgDAPEP, which has a side chain that faces away from the active site cavity – unlike the glutamine, which has a side chain facing towards the active site cavity.
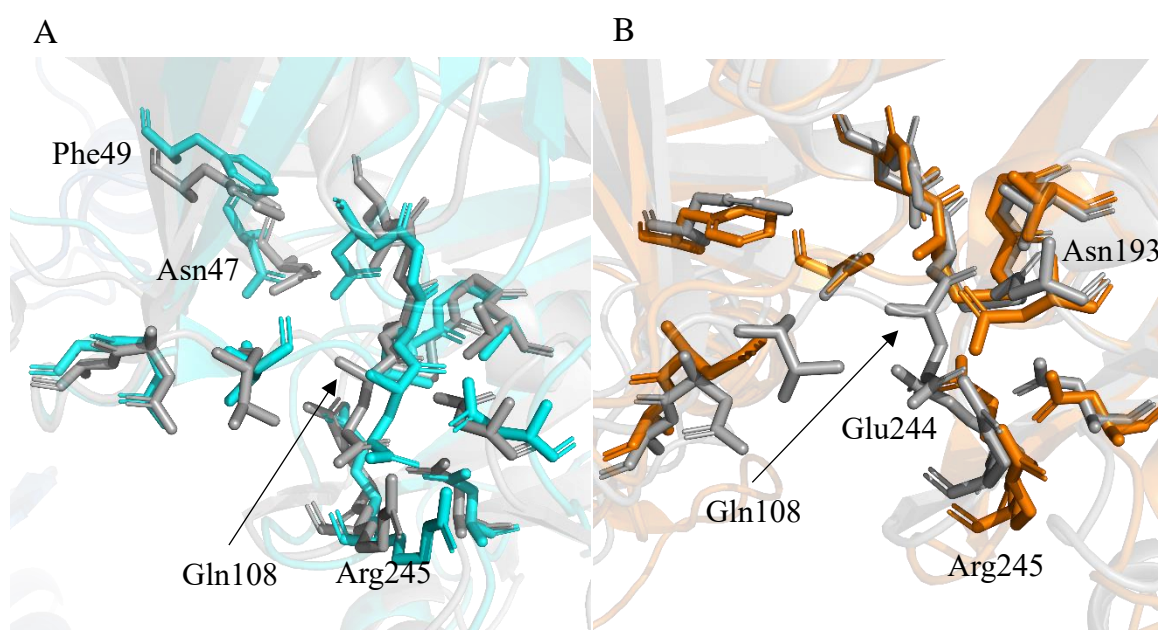
Figure 21. Positioning analysis of PaDAPEP active site residues. (A) PaDAPEP active site residues (grey) superimposed over HiDAPEP (1GQZ) active site residues (cyan), resulting in an RMSD of 1.5 Å (15 α-carbon pairs). **(B)** PaDAPEP active site residues (grey) overlayed with CgDAPEP (5H2G) active site residues (orange) resulting in a root-mean-square deviation (RMSD) of 0.86 Å (14 α-carbon pairs). Images generated using PYMOL (version 4.6).

4.3.6 Dimerisation Interface

Given the dimerisation of DAPEP has been shown to be essential for its catalytic activity (Hor *et al*, 2013), the interface at which this occurs is a promising antibiotic target. A Proteins, Interfaces, Structures, and Assemblies (PISA) analysis was conducted to identify this interface

and highlight residues that could be targeted in PaDAPEP. The PISA analysis revealed that the dimerisation interface of PaDAPEP buries 755 $\mathring{A}^2$ per monomer, which is equal to 6.1% of the total protein surface area (Figure 21A). There are three major chains in each monomer where this occurs: at the N-terminal from residues 36 to 48, residues 72-79 and at the C-terminal from residues 302 to 309. Furthermore, the analysis identified residues Asn73, Glu305 and Gly307 in monomer A and residues Asp48, Glu305 and Gly307 in monomer B as hydrogen bond forming, which anchor the monomers together and oligomerise the protein. Interestingly, the same analysis of DAPEP from the Gram-negative species examined in Section 4.3.4, indicates a higher degree of hydrogen bonding between the monomers of each orthologue when compared to PaDAPEP. In *A. baumannii, E. coli* and *H. influenzae*, there were 7, 19 and 9 hydrogen bonds involved in complex formation, respectively. Additionally, comparison of these analyses revealed that there were no consistent hydrogen bond networks between specific residues in each protein. There was, however, consistency in amino acid positioning of the hydrogen bonds as each orthologue had residues forming a hydrogen bond between positions equivalent to 305 and 307 in PaDAPEP.
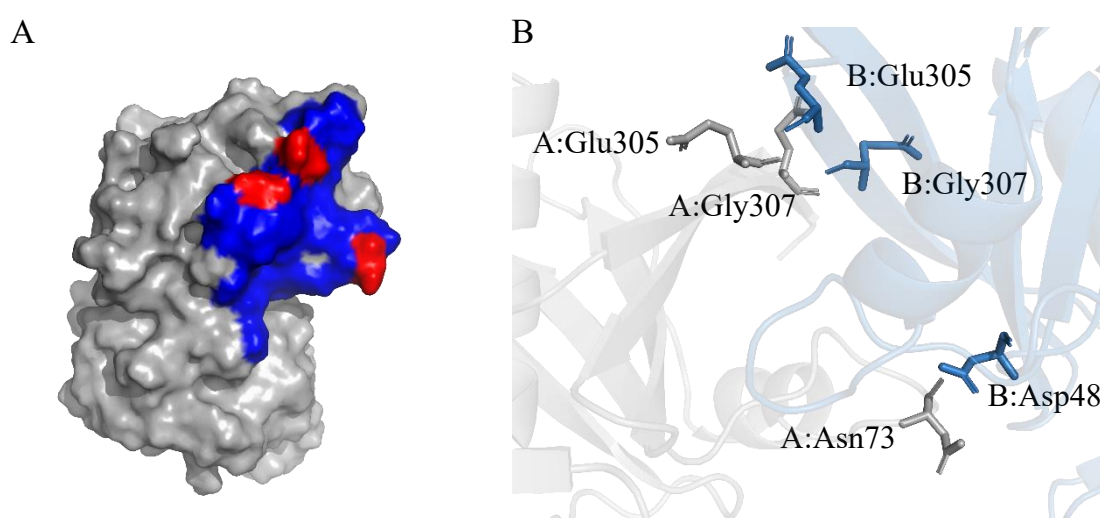
Figure 22. PaDAPEP dimerisation interface. (A) Surface representation of the monomer A (grey) dimerisation interface residues (blue) and the hydrogen bond forming residues (red). **(B)** Positioning of the hydrogen bond forming residues in both monomers within the dimerisation interface. Images generated using PYMOL (version 4.6).

4.4   Summary

Characterisation of recombinant PaDAPEP was carried out in solution using CD spectroscopy and AUC, demonstrating that the enzyme predominantly forms β-structures and exists as a dimer. Crystallisation conditions for the protein were identified and optimised to produce diffractable crystals. Subsequently, the crystal structure of PaDAPEP was solved to 1.74 Å, revealing a tertiary structure that adopts the conserved 'DAP epimerase-like' fold. Using the solved crystal structure, specific amino acids within the dimerisation interface of PaDAPEP were identified as potential targets for drug development and the active site was characterised to guide future structure-based discovery efforts.

Chapter Five

Discussion

5.1   Introduction

Antibiotic resistance is rapidly disseminating worldwide and threatens the efficacy of antibiotics that are critical for modern medicine (Spellberg & Gilbert, 2014). This crisis has been exacerbated by the lack of antibiotic development, particularly against Gram-negative pathogens (Renwick & Mossialos, 2018). *P. aeruginosa* is the highest priority bacteria according to the WHO that requires the urgent development of new antibiotics (World Health Organisation, 2014). Thus, there is a critical need to investigate novel targets for antipseudomonal drugs. DAPEP represents a promising target, as it is responsible for the production of *meso*-DAP, which is a constituent of peptidoglycan in the bacterial cell wall and can be irreversibly decarboxylated to form the amino acid lysine. This thesis sought to provide detailed insights into the enzyme DAPEP from *P. aeruginosa* to investigate its potential as a novel antibiotic target. Characterisation of PaDAPEP was completed to determine its structure and catalytic parameters, which will facilitate future experiments within the antibiotic discovery pipeline. Furthermore, steps towards generating a *dapF* deletion mutant in *P. aeruginosa* were made to assess the effect of *meso*-DAP depletion on bacterial survival and growth.

5.2   Establishing a Genetic Tool to Assess *meso*-DAP Depletion

As discussed in Section 1.4, there has been no investigation to characterise the effect of *meso*-DAP depletion on GNB. Hence, this study aimed to introduce a direct deletion of the *dapF* gene into the *P. aeruginosa* genome to determine the importance of *meso*-DAP for bacterial survival and growth. Gene knockouts have long been considered more difficult in *P. aeruginosa*, compared to other bacterial species, due to the inefficiency and time dedication of the established lambda red system commonly used for *E. coli*. Recently, a streamlined method was developed by Huang and Wilks (2017) using a double homologous recombination event with a suicide vector utilising *sacB* for counterselection. As such, this approach was followed to introduce the *dapF* deletion into the *P. aeruginosa* genome.

In this study, the suicide vector was cloned by amplifying the 500 bp regions upstream and downstream of the *dapF* gene, using primers that introduced ends complementary to each region and the pEX18Tc vector. This facilitated the subsequent Gibson assembly, successfully ligating the vector in preparation for its transformation into *P. aeruginosa*, and integration into the genome. Attempts to transform the construct into *P. aeruginosa* were conducted using three transformation protocols that have previously displayed efficacy in *P. aeruginosa*: (i) electroporation, (ii) conjugation and (iii) heat shock (Huang & Wilks, 2017; Hmelo *et al*, 2015; Chuanchuen *et al*, 2002). However, these transformation conditions were unsuccessful, despite extensive optimisation and troubleshooting.

Undoubtedly, the most utilised transformation method in this study was electroporation. Initially, cell lysis was observed using the electroporation conditions from Huang and Wilks (2.2 kV, 15 ms and 600 Ω). This was likely due to the pulse length being significantly higher (15.0 ms) than what was reported (4.0 – 4.5 ms), as once pulse length was adjusted to be consistent with conditions from other papers, the visible cell lysis disappeared (Iwasaki *et al*, 1994; Shen *et al*, 2006). Other attempts to optimise the electroporation conditions included

49

changes in the overnight incubation temperature of the bacteria, use of more enriched rescue media and supplemented plates, however, no integration of the plasmid was observed. Other transformation methods, such as conjugation and heat shock, were also employed to transform the suicide vector into *P. aeruginosa*. For the conjugation protocol, while initial transformation of the donor *E. coli* strain with the suicide plasmid was successful, it did not yield any successful transformants. Similar results were observed using heat shock. Given that three different transformation techniques were used, which have previously displayed efficacy in *P. aeruginosa*, it is likely that the problem lies within the integration of the plasmid, rather than its transformation into the cell. This is further supported by the fact that the suicide vector was both re-sequenced and re-made over the course of the project. This ensured that no mutations were introduced when replicating the plasmid, which could have, for example, disrupted the tetracycline resistance gene used for selection, or the complementary DNA regions that facilitate integration into the *P. aeruginosa* genome. Interestingly, the *dapF* gene falls within an operon of six proteins, four with known activity and two conserved hypothetical proteins (Mao *et al*, 2009). Hence, it may be possible that the integration is working, however, the plasmid is disrupting expression of the entire operon, which is resulting in the bacteria's inability to grow.

Successfully integrating the suicide vector into the *P. aeruginosa* genome will overcome the major hurdle required to generate a *dapF* deletion in *P. aeruginosa*, which will be used to determine the importance of *meso*-DAP to bacterial viability. If the deletion results in nonviable bacteria, supplementation experiments with *meso*-DAP could be performed to allow for the minimum amount of *meso*-DAP required for bacterial growth to be determined. Additionally, a deletion mutant could also be utilised in an *in vivo* infection model to study the effect of *meso*-DAP depletion on bacterial virulence, allowing for preliminary data to be gathered on the potential efficacy of future DAPEP inhibitors. Furthermore, this mutant will also validate

PaDAPEP as an antibiotic target, if deemed essential. The possibility of the *dapF* gene in *P. aeruginosa* being non-essential must also be considered. In this case, the extensive target characterisation completed in this study is still important, as the gene deletion could result in a fitness cost for the bacteria. Therefore, the deletion mutant must still be assessed for disadvantages induced by the deletion, such as an inability to form biofilms, increased antibiotic susceptibility, decreased virulence or attenuated growth. These disadvantages must be examined to elucidate whether inhibitors of the target of interest would be stand-alone antibacterial agents or function as adjuvant therapies to enhance the activity of current antibiotics. Importantly, anti-virulence factor antibiotics offer an alternative approach for host defence from pathogenic bacteria by inhibiting their ability to invade, cause disease and persist (Defoirdt, 2018). This type of inhibition is particularly advantageous, as it does not kill pathogens, therefore avoiding the strong selective pressures that promote the development of antibiotic resistance from traditional antibiotic treatments (Fleitas Martínez *et al*, 2019).

5.3   Production of Recombinant PaDAPEP

To overexpress and purify PaDAPEP for the first time, a pET28a-*dapF* protein expression vector was designed and cloned. The gene was amplified from *P. aeruginosa* PAO1 genomic DNA by PCR, employing Phusion high-fidelity DNA polymerase to ensure no mutations were introduced into the product. The expression vector was successfully ligated by T4 DNA ligase, after which it was transformed into *E. coli* BL21 (DE3) cells to overexpress PaDAPEP. The recombinant enzyme was purified to yield >30 mg of protein per litre of expression culture at ~99% purity. Producing recombinant PaDAPEP at high yield and purity for the first time permitted extensive characterisation of the enzyme to facilitate the future design and testing of inhibitors that target it.

5.4 Characterising the Catalytic Parameters of PaDAPEP

The catalytic parameters of PaDAPEP were determined using the DAPEP-DAPDH coupled assay (Cox *et al*, 2000). An initial rate versus substrate concentration assay was completed to determine a concentration that ensured a measurable rate for subsequent kinetic analysis of the PaDAPEP enzyme. Given these results, the enzyme was tested at a concentration of 63 nM to determine the Michaelis-Menten parameters, K_M and k_{cat}. The binding affinity for L,L-DAP (K_M) was measured to be 0.14 ± 0.03 mM, while its catalytic turnover (k_{cat}) was 127 ± 6 s^{-1}. Compared to the two previous studies that have evaluated these parameters in DAPEP from other bacterial species, these vary significantly, with only some similarities observed in k_{cat}. In CgDAPEP, K_M was 1.9 mM and k_{cat} was 58 s^{-1}, while in HiDAPEP, K_M was 0.70 ± 0.1 mM and k_{cat} was 128 ± 3 s^{-1} (Koo & Blanchard, 1999; Sagong & Kim, 2017). This indicates that PaDAPEP has a higher affinity for the substrate as it requires significantly less L,L-DAP to become saturated and reach its maximal velocity (V_{max}). It should be noted that variability in K_M values for enzymes involved in the same reaction, within different organisms, is not uncommon (Robinson, 2015). This is likely due to primary and tertiary structure nuances that exist between orthologous proteins. In the case of PaDAPEP and its orthologues, some of these nuances were observed in Section 4.3.5. Structural alignments identified a positioning bias of the active site residues towards the active site cleft, which could increase the molecular contacts within the active site, resulting in a more extensive hydrogen bonding network with the substrate. Hence, PaDAPEP's affinity for L,L-DAP would increase, resulting in a lower K_M value. Substitution of the highly conserved active site residue, Glu108, for a methionine was also observed in CgDAPEP (Pillai *et al*, 2006). This is likely a contributor to the significantly lower K_M of CgDAPEP, compared to PaDAPEP, as the residue forms part of an extensive network of hydrogen bonds within the active site cleft. Therefore, the substitution could be disrupting this hydrogen bonding network and, consequently, reducing the affinity of

CgDAPEP for its substrate. Importantly, the variation in kinetic parameters resulting from these nuances can be exploited to design DAPEP inhibitors with improved potency against specific bacterial species. Furthermore, understanding these values is important for future inhibitor characterisation, as they allow the inhibitor's effect on the catalytic activity of PaDAPEP to be quantitatively assessed.

5.5 Identification of PaDAPEP Inhibition Sites

To identify inhibition sites in PaDAPEP, the initial steps of a structure-based inhibitor discovery program were completed using in solution structural biology techniques and X-ray crystallography. CD spectroscopy confirmed the correct folding of the enzyme and revealed a secondary structure composition that is consistent with DAPEP from *E. coli*, *C. glutamicum, M. tuberculosis* and *H. influenzae* (Hor *et al*, 2013; Sagong & Kim, 2017; Cirilli *et al*, 1998; Usha *et al*, 2009). AUC was performed to elucidate the quaternary structure of PaDAPEP in solution. Sedimentation velocity experiments indicated the enzyme forms a dimer, which further supports findings from site-directed mutagenesis experiments in *E. coli* DAPEP show that the dimerisation of the enzyme is essential for its catalytic activity (Hor *et al*, 2013). Similar experiments will need to be conducted with PaDAPEP to confirm this hypothesis. Such studies would further highlight that disrupting the quaternary structure of PaDAPEP represents a promising strategy for inhibition of the enzyme. X-ray crystallography was subsequently employed to determine the enzyme's structure at the atomic level and provide valuable information on potential druggable sites. The apo structure of PaDAPEP was solved to 1.74 Å. Importantly, each of the monomers adopted the characteristic 'epimerase-like' fold that is observed in DAPEP orthologues and conserved among some amino acid racemase and isomerase proteins (Buschiazzo *et al*, 2006; Garvey *et al*, 2007; Parsons *et al*, 2004; Velarde *et al*, 2009; Blankenfeldt *et al*, 2004; Grassick *et al*, 2004; Liger *et al*, 2005). The crystal structure

also confirms the data from the in-solution characterisation, as it crystallised as a dimer and predominantly formed β structures. Most pertinent to this project, analysis of the structure facilitated the identification and characterisation of specific sites for inhibitor development. In particular, the hydrogen bond forming residues responsible for dimerisation of PaDAPEP and the active site. These insights will provide important information for future structure-based discovery efforts, which will be discussed in Section 5.6. Structural similarities of DAPEP among Gram-negative pathogens were also analysed, initially through structural alignment of the enzymes and then by PISA analysis. As expected, there was a high degree of structural conservation between the DAPEP orthologues, however, the PISA analysis indicated variability among the dimerisation interfaces. This suggests that antibacterial compounds targeting the dimerisation interface would likely be narrow-spectrum, i.e., would be specific for a particular species. Conversely, given that the active site of DAPEP is largely conserved in bacteria, active site inhibitors would likely have broad-spectrum activity, displaying efficacy in several GNB. This makes them particularly useful when the species of bacteria causing an infection is unknown. In these cases, empirical treatment with broad-spectrum antibiotics allows for appropriate action to be taken, while the infecting pathogen is determined (Kollef, 2008). However, this type of therapy has its drawbacks, as it indiscriminately targets pathological bacteria and naturally occurring bacterial flora, which can disrupt the gut microbiome, facilitating the colonisation of resistant pathogenic bacteria (Yang *et al*, 2018). On the other hand, narrow-spectrum antibiotics – such as a PaDAPEP dimerisation interface inhibitor – target specific species, making them highly sought after as they reduce the emergence of resistance and result in less collateral damage to the gut microbiome due to their specificity (Alm & Lahiri, 2020). Developing both broad- and narrow- spectrum antibiotics is essential for clinical application, as the two are often used in conjunction with each other (Kollef, 2008). This ensures that the shortest duration of therapy is possible, and subsequently,

minimises the potential for resistance to emerge. The potential for development of both broad- and narrow-spectrum antibiotics targeting DAPEP is an exciting prospect, given their unique advantages.

5.6   Inhibition of PaDAPEP

Currently, inhibition of DAPEP has only been achieved through active site inhibitors (Pillai *et al*, 2007; Usha *et al*, 2008; Caplan *et al*, 2000). Many of these inhibitors share structural similarities with *meso*-DAP and act by binding to the catalytic cysteine residues, rendering the enzyme inactive. However, none of these inhibitors have reported antibacterial activity against intact bacteria. The discovery that dimerisation of bacterial DAPEP is required for its catalytic activity (Hor *et al*, 2013), has opened unexplored opportunities for inhibition of the enzyme. The potential druggable sites of PaDAPEP presented in this thesis provides a strong basis for the development of protein-protein interactions modulators, which, in the case of PaDAPEP, would inhibit its activity by disrupting the enzyme's quaternary structure. A similar approach has already displayed efficacy inhibiting HIV-1 integrase, an enzyme important for integrating viral DNA into a host, and as an antifungal drug (Lockhart *et al*, 2020; Zhao & Chmielewski, 2013). Additionally, the active site of PaDAPEP also represents an attractive target for structure-based inhibitor discovery, as active site inhibitors against the enzyme already display *in vitro* efficacy.

To design inhibitors of PaDAPEP in the future, we can use the crystal structure from this study to screen libraries of compounds or fragments *in silico*, and identify scaffolds that could be optimised for the development of antibacterial agents. The structure will also enable us to characterise hits using co-crystallisation and inhibitor soaking approaches. These methods play an essential role in drug discovery, as they provide an understanding of the structure-activity relationship and mechanism of action of inhibitors, which can be used to design more potent

analogues. These studies would also benefit from having solved crystal structures of PaDAPEP in different conformations. This is because enzymes are intrinsically dynamic and crystal structures only provide a static perspective on an enzyme. Therefore, having solved crystal structures of PaDAPEP in the reduced conformation and with substrate bound, for example, would provide a greater overall understanding of its structural dynamics.

5.7   Conclusion

In conclusion, this study provides the first steps towards establishing a genetic tool to knockout the DAPEP encoding gene in *P. aeruginosa* to conclusively assess the importance of *meso-*DAP to bacterial viability and growth. Moreover, it provides structural and functional insights into *P. aeruginosa* DAPEP that could pave the way for future work aimed at developing inhibitors that are effective against multi-drug resistant strains of *P. aeruginosa*.

Chapter Six

Materials and Methods

6.1 Materials

Unless otherwise stated, chemical reagents used to complete the experiments were sourced from Sigma Aldrich, Astral Scientific or Hampton Research. Primers were purchased from Bioneer Pacific. DNA and protein standards, including the 1 kb Plus DNA Ladder and Unstained Protein Standard, Broad Range (10-200 kDa), were sourced from New England Biolabs (NEB). Protein purification was carried out in the Next Generation Chromatography system with 5 mL Bio-Scale™ Mini Nuvia™ IMAC columns that were purchased from BioRad. *P. aeruginosa* PAO1 cells and purified pEX18Tc plasmid were kindly supplied by Dr Rachel Impey (La Trobe University, Australia). The pET28a expression vector was provided by Dr Sebastien Desbois (La Trobe University, Australia). Stocks of *E. coli* BL21 (DE3) cells transformed with the pET11a expression vector harbouring the gene encoding *C. glutamicum* DAPDH were provided by Ms Emily Mackie (La Trobe University, Australia). *E. coli* S17.1 cells were generously provided by Assoc Prof Steve Petrovski (La Trobe University, Australia).

6.2   Methods

6.2.1   General Methods

6.2.1.1 Competent Cell Preparation

All *E. coli* cells used (DH5α, BL21 (DE3) and XL1-Blue) were made competent using an altered version of the CaCl$_2$ method from Sambrook & Russell (2001). Specifically, *E. coli* cells from frozen glycerol stocks were inoculated in 5 mL of LB media and grown overnight at 37 °C. Subsequently, 50 mL of LB media were inoculated with 500 µL of the overnight culture and grown to an optical density at 600 nm (OD$_{600}$) of 0.4 – 0.6. Cells were then placed on ice for 10 min and centrifuged (2000 × g, 10 min, 4 °C). The pellet was resuspended in 10 mL of ice cold 0.1 M CaCl$_2$ and incubated on ice for 30 min. The cells were once again centrifuged (2000 × g, 5 min, 4 °C) and the pellet resuspended in ice cold 0.1 M CaCl$_2$ and 20% (v/v) glycerol up to 2 mL. The resuspension was aliquoted into 50 µL fractions, snap frozen in liquid nitrogen and stored at -80 °C.

6.2.1.2 Transformation of Competent *E. coli* Cells

Transformation of competent *E. coli* cells was completed via a heat shock protocol according to Sambrook & Russell (2001). Briefly, frozen competent cells were thawed on ice and treated with at least 1 µL of plasmid DNA (>2 ng), followed by an incubation on ice for 20 min. Cells were then subjected to heat shock at 42 °C for 45 s and immediately placed back on ice for a further 5 min. The cells were rescued in 0.7 mL of LB media and subsequently incubated for 1 h at 37 °C without shaking. All cells were plated on LB agar plates containing the appropriate antibiotics and incubated overnight at 37 °C.

6.2.1.3 Bacterial Glycerol Stock Preparation

A single bacterial colony was inoculated into 10 mL of LB media containing the appropriate antibiotics, followed by an overnight incubation at 37 °C. Subsequently, 500 µL of the overnight culture was added to 500 µL of 50% (v/v) glycerol before snap freezing and storage at -80 °C.

6.2.1.4 Agarose Gel Electrophoresis

Agarose gel electrophoresis was conducted using 1% (w/v) agarose gels stained with 1% (v/v) GelGreen (Fisher Biotech) as previously specified (Sambrook & Russel, 2001). Samples were combined with 6× loading dye (NEB) prior to loading onto a gel and a 1 kb DNA ladder (NEB) was used as the molecular weight standard. Agarose gels were placed within a Mini-Sub Cell GT Electrophoresis system (Bio-Rad) filled with 1 × Tris-acetate ethylenediaminetetraacetic acid buffer and were run at 90 V for 50 min. Gels were imaged using the GeneSys system (Syngene).

6.2.1.5 Tris-Glycine SDS-PAGE

SDS-PAGE was carried out on 12% (w/v) polyacrylamide gels according to a previously established protocol (Sambrook & Russel, 2001). A 2× SDS-PAGE reducing loading dye was combined with each sample prior to loading and molecular weight was estimated using Unstained Protein Standard, Broad Range (10-200 kDa) (NEB). Electrophoresis was conducted at 160 V for 50 min using a Mini-Protean II system (Bio-Rad). Gels were stained with Coomassie Brilliant Blue R-250 for 30 min and de-stained with 30 % (v/v) methanol and 10 % (v/v) acetic acid for 2 h. Gels were imaged using a GeneSys system (Syngene).

6.2.1.6 Sequencing

Plasmids were sent for Sanger sequencing at the Australian Genome Research Facility (Victorian Comprehensive Cancer Centre, Melbourne). Approximately 800 ng of plasmid was utilised for sequencing using the appropriate primers from Table 3. The sequencing results were analysed on SnapGene (GSL Biotech).

Table 3. Primer list. Lowercase bases represent overlapping regions required for cloning as described in Section 6.2.2.3.

Primer	Primer Sequence (5'-3')
(1) Upstream Fwd	cagctatgaccatgattacgCGACTACATCCGCGCCATC
(2) Upstream Rev	gcgacggcccGGTCTGGGCCTCACTGCG
(3) Downstream Fwd	ggcccagaccGGGCCGTCGCCCGCGAGA
(4) Downstream Rev	atccccgggtaccgagctcgAACGCCGCAGACGGTCTTGCC
(6) pEX18Tc Universal Fwd	GGCTCGTATGTTGTGTGGAATTGTG
(7) pEX18Tc Universal Rev	GGATGTGCTGCAAGGCGATTAAG
(8) *dapF* Fwd	GTATCCGGATCCATGCTTTTGCGCTTCACCAAGATG
(9) *dapF* Rev	GTACCAAAGCTTGGCCCTTACAGGCGGACC
(10) T7 Promoter Fwd	TAATACGACTCACTATAGGG
(11) T7 Terminator Rev	CTAGTTATTGCTCAGCG
(12) Upstream gDNA	CGGCAAGGCATCGGCATTC
(13) Downstream gDNA	CAGAGGGACTCAAAGGTCCCTGAC

6.2.2 Gene Deletion Methods

6.2.2.1 pEX18Tc Plasmid Preparation

E. coli DH5α cells transformed with the pEX18Tc plasmid as detailed in Section 6.2.1.2 were plated on tryptic soy agar (TSA) media containing 10 µg/mL of tetracycline and incubated overnight at 37 °C. A single colony was subsequently inoculated in 10 mL of similarly supplemented LB media and incubated at 37 °C overnight. Plasmid DNA was purified using the *AccuPrep*® Nano-Plus Plasmid Mini Extraction Kit (Bioneer) and the concentration measured using an ND-1000 Spectrophotometer (Thermo Scientific) before storage at -30 °C.

6.2.2.2 Restriction Digest of pEX18Tc Plasmid

Purified pEX18Tc plasmid (Section 6.2.2.1) was digested using EcoRI-HF (NEB) in accordance with the manufacturer's protocol, with the inclusion of 1 µL of shrimp alkaline phosphatase. Successful digestion was confirmed using agarose gel electrophoresis (Section 6.2.1.4).

6.2.2.3 Primer Design

Primers were designed with a sequence complementary to regions flanking the *dapF* gene (uppercase) to amplify 500 bp DNA fragments upstream and downstream of the gene (primers 1 - 4, Table 3). Importantly, each primer was also designed with complementary overlapping bases (lowercase) to facilitate a subsequent Gibson assembly of the upstream and downstream fragments into the pEX18Tc plasmid (Section 6.2.2.5).

6.2.2.4 Colony PCR Fragment Amplification

The upstream and downstream fragments were prepared by resuspending a single colony of *P. aeruginosa* PAO1 cells in 50 µL of nuclease-free water. Subsequently, 50 µL reactions were aliquoted from a PCR master mix – the components of which can be seen in Table 4 – and amplified in a T100 Thermal Cycler (Bio-Rad) using the conditions in Table 5. The product size was analysed by agarose gel electrophoresis (Section 6.2.1.4). The Monarch® PCR DNA Cleanup Kit (NEB) was then utilised to purify the upstream and downstream fragments, which were stored at -30 °C.

Table 4. Colony PCR master mix components.

Component	Reaction Master Mix (µL)
Forward primer	2
Reverse primer	2
One*Taq*® 2× Master Mix with Standard Buffer	50
Template DNA	6
Nuclease-free H_2O	40
Total	100

Table 5. Thermal cycler amplification conditions.

Step		Temperature (°C)	Time (min)
Initialisation		95	15
Denaturation	× 35 cycles	95	0.5
Annealing		62.5	0.5
Elongation		68	1.5
Final Elongation		68	5

6.2.2.5 Plasmid Assembly

Upstream and downstream fragments (Section 6.2.2.4) were assembled into the digested pEX18Tc vector (Section 6.2.2.2) by Gibson assembly, using the NEBuilder® HiFi DNA Assembly Master Mix (NEB) as per manufacturer's protocol. The assembled plasmid was then transformed into competent *E. coli* DH5α cells (Section 6.2.1.1) and plated on TSA media containing 10 µg/mL of tetracycline, which were incubated at 37 °C overnight. A 10 mL culture of LB media supplemented with tetracycline was inoculated with a single colony of transformants and incubated overnight at 37 °C. The plasmid was isolated using the *AccuPrep®* Nano-Plus Plasmid Mini Extraction Kit (Bioneer) and the concentration measured spectrophotometrically using an ND-1000 Spectrophotometer (Thermo Scientific). Following confirmation by Sanger sequencing employing primers 6 and 7 (Table 3), the assembled plasmid was stored at -30 °C.

6.2.2.6 Optimisation of Transformation Conditions

6.2.2.6.1 Electroporation

The first method employed to transform the assembled plasmid into *P. aeruginosa* PAO1 was electroporation, as described by Huang & Wilks (2017). Briefly, a colony of *P. aeruginosa* PAO1 was inoculated in 5 mL of LB media and grown overnight at 42 °C without shaking. Cells were harvested from 4 mL of the overnight culture by centrifugation (13000 × g, 1 min, 21 °C) and the pellet resuspended in 1 mM $MgSO_4$. This wash step was repeated a further 3 times, after which the cells were resuspended in 50 µL of 1 mM $MgSO_4$. The cell suspension was then mixed with 10 µg of the purified suicide vector and transferred to a 2 mm gap electroporation cuvette (Bio-Rad). Electroporation was carried out employing a range of conditions, as listed in Table 1, using a Gene Pulser Xcell (Bio-Rad). Following electroporation, cells were immediately rescued with 1 mL of LB before being incubated for 3

h at 37 °C with shaking. All cells were plated on LB agar supplemented with 100 µg/mL tetracycline and incubated at 37 °C for 48 h.

6.2.2.6.2 Conjugation

The second transformation method utilised a modified conjugation protocol from Hmelo *et al* (2015) and Aparicio *et al* (2019). Initially, a donor *E. coli* strain S17.1 was transformed with the suicide vector by electroporation. To achieve this, a 10 mL LB media culture of *E. coli* S17.1 was prepared and incubated overnight at 37 °C with shaking. Subsequently, 500 µL of the overnight culture was used to inoculate 5 mL of LB media and grown to an OD_{600} of 0.5 – 0.6. An aliquot of the cells (2 mL) was then centrifuged (10000 × g, 2 min, 4 °C) and resuspended in 1 mL of ice cold 10% (w/v) glycerol. This wash step was repeated once again, and the cells subsequently resuspended in 20 µL of ice cold 10% (w/v) glycerol. Following resuspension, 200 ng of purified suicide vector was added to the mixture and electroporation (1.8 kV, 25 µF, 200 Ω) carried out in a pre-chilled 1 mm gap electroporation cuvette (Bio-Rad). Cells were immediately rescued with 500 µL of SOC media and incubated for 1 h at 37 °C. A 50 µL aliquot of the culture was then plated on LB agar supplemented with 10 µg/mL tetracycline and incubated at 37 °C for 24 h.

To allow for transformation of the suicide plasmid, 5 mL of LB media overnight cultures of the transformed *E. coli* strain (10 µg/mL tetracycline supplementation) and *P. aeruginosa* PAO1 (no antibiotic supplementation) were prepared and incubated at 37 °C with shaking. Following an overnight incubation, the PAO1 culture was transferred to a 42 °C incubator for 3 h. Subsequently, 800 µL of each overnight culture was collected by centrifugation (9300 × g, 2 min, 21 °C) and each pellet resuspended in 800 µL of 10 mM $MgSO_4$. The wash step was repeated once more, followed by mixing 200 µL of each resuspension and centrifugation (9300 × g, 2 min, 21 °C). The 'mating mixture' was resuspended in 20 µL of 10 mM $MgSO_4$ and

spotted onto an LB agar plate that was incubated at 30 °C overnight. The spot was then scraped off the plate, resuspended in 1 mL of 10 mM MgSO$_4$ and plated onto M9 minimal media plates supplemented with 0.2% (w/v) citrate and 100 μg/mL tetracycline, which was incubated at 30 °C overnight.

6.2.2.6.3 Chemical Transformation

The preparation of chemically competent *P. aeruginosa* PAO1 cells follows a previously described protocol (Chuanchuen *et al*, 2002), beginning with the inoculation of 4 mL of LB media with a colony of *P. aeruginosa* PAO1 cells that were incubated overnight at 37 °C with shaking. The cells were collected by centrifugation (13000 × g, 30 sec, 21 °C) and resuspended in 1 mL of ice cold 0.1 M MgCl$_2$ while on ice. This centrifugation was repeated to collect the cells and they were resuspended in 1 mL of ice-cold transformation (TG) salts (75 mM CaCl$_2$, 6 mM MgCl$_2$, 15% (w/v) glycerol). The cell suspension was incubated on ice for 10 min and centrifuged (13000 × g, 30 sec, 21 °C). Finally, the cells were resuspended in 200 μL of TG salts rendering them chemically competent. Aliquots (100 μL) of the chemically competent cells were then mixed with 1 μg of the purified suicide vector and incubated on ice for 15 min. The suspension was heat shocked at 37 °C for 2 min and immediately rescued with 500 μL of LB media before being incubated at 37 °C for 1 h with shaking. All cells were plated on LB agar supplemented with 100 μg/mL tetracycline and incubated at 37 °C for 24 h.

6.2.3 Protein Biochemistry Methods

6.2.3.1 pET28a Plasmid Preparation

E. coli XL1-Blue cells containing the pET28a plasmid were incubated overnight at 37 °C with shaking, following inoculation in 10 mL of LB and 50 µg/mL kanamycin. The *AccuPrep®* Nano-Plus Plasmid Mini Extraction Kit (Bioneer) was used to extract the plasmid following manufacturer's instructions. The concentration was measured using an ND-1000 spectrophotometer (Thermo Scientific) and plasmid was stored at -30 °C.

6.2.3.2 pET28a Plasmid Restriction Digestion

Purified pET28a plasmid was digested with BamHI-HF and HindIII-HF (NEB) in accordance with the manufacturer's protocol. To confirm digestion, the plasmid was subjected to agarose gel electrophoresis (Section 6.2.1.4).

6.2.3.3 Amplification of *dapF* Insert

Forward and reverse primers were designed with regions complementary to the *dapF* gene that included BamHI and HindIII restriction sites on the 5' ends, respectively (primers 10 and 11, Table 3). *P. aeruginosa* PAO1 genomic DNA was used as a PCR template and prepared with the *AccuPrep®* Genomic DNA Extraction Kit (Bioneer) and stored at -30 °C. Two 50 µL reactions were aliquoted from a PCR master mix – detailed in Table 6, which were amplified in a T100 Thermal Cycler (Bio-Rad) using the conditions listed in Table 7. Subsequently, 25 µL of the product was analysed via agarose gel electrophoresis (Section 6.2.1.4). The *dapF* insert was then purified from the remaining 75 µL using the Monarch® PCR DNA Cleanup Kit (NEB) and stored at -30 °C.

Table 6. PCR master mix components.

Component	Reaction Master Mix (µL)
Phusion® HF buffer (5×)	20
Deoxyribonucleotide triphosphate (10 mM)	4
Forward primer	2
Reverse primer	2
Phusion® High-Fidelity DNA Polymerase	1
P. aeruginosa PAO1 genomic DNA template	6
Nuclease-free H_2O	65
Total	100

Table 7. Thermal cycler PCR conditions.

Step		Temperature (°C)	Time (min)
Initialisation		95	5
Denaturation	× 35 cycles	95	0.5
Annealing		62.5	0.5
Elongation		72	1
Final Elongation		72	5

6.2.3.4 T4 DNA Ligation

Purified *dapF* insert (1 µg) was first subjected to restriction digest by the enzymes BamHI-HF and HindIII-HF (NEB) using the protocol from Section 6.2.3.2 for ligation. Following this, the *dapF* insert was purified using the Monarch® PCR DNA Cleanup Kit (NEB) and subsequently ligated into digested pET28a plasmid with the T4 DNA Ligase (NEB), according to the manufacturer's protocol. The ligated expression vector was transformed into competent *E. coli*

XL1-Blue cells (Section 6.2.1.1) and plated on TSA plates supplemented with 50 µg/mL kanamycin. Transformants were selected and the colony used to inoculate 10 mL of LB media also containing 50 µg/mL kanamycin and incubated overnight at 37 °C. The *AccuPrep®* NanoPlus Plasmid Mini Extraction Kit (Bioneer) was used to purify the pET28a-*dapF* plasmid from the overnight culture and the concentration measured using an ND-1000 spectrophotometer (Thermo Scientific). The integrity of the plasmid was confirmed by Sanger sequencing, as detailed in Section 6.2.1.6, using primers 10 and 11 (Table 3). The plasmid was stored at 30 °C.

6.2.3.5 PaDAPEP Protein Expression

After transformation of the pET28a-*dapF* protein expression vector into *E. coli* BL21 (DE3), as per Section 6.2.1.2, a 10 mL culture of LB media containing 50 µg/mL of kanamycin was inoculated with the transformed cells and incubated overnight at 37 °C with shaking. Three 50 mL cultures of LB supplemented with 50 µg/mL of kanamycin were inoculated with a 1 mL aliquot from the overnight culture and grown to an OD_{600} of $0.6 - 0.8$. Once each 50 mL culture reached the target OD_{600}, 1 mM of IPTG was added to induce expression of the PaDAPEP protein. The flasks were kept at varying temperatures with shaking at 160 rpm, which included 16 °C for 24 h, 25 °C for 20 h and 37 °C for 4 h. Cells were harvested by centrifugation (5000 $\times$ g, 30 min, 4 °C) and the pellets stored at -30 °C. The cell pellets were then thawed on ice, resuspended in 10 mL of Buffer A (Table 8) and sonicated on ice in a Misonix Ultrasonic Liquid Sonicator (40 mA, 5 s ON time, 30 s OFF time for 90 s total ON time). The fractions were analysed via SDS-PAGE (Section 6.2.1.5) to determine the optimal temperature for protein expression. *E. coli* BL21 (DE3) cells transformed with the expression vector were incubated in 50 mL LB cultures supplemented with 50 µg/mL kanamycin at 37 °C overnight with shaking at 160 rpm. Cultures (25 mL) were used to inoculate 1 L of supplemented LB

media, which was incubated at 37 °C with shaking and grown to an OD_{600} of 0.6 – 0.8. Protein expression was induced with the addition of 1 mM IPTG and the expression culture was incubated at 16 °C for 24 h with shaking at 160 rpm. The cells were harvested by centrifugation ($5000 \times g$, 30 min, 4 °C) and the pellets stored at -30 °C.

6.2.3.6 DAPDH Protein Expression

To express the coupling enzyme required for the DAPEP kinetic assay, DAPDH, *E. coli* BL21 (DE3) cells were transformed with the pET11a-*ddh* expression vector as per Section 6.2.1.2. Cells transformed with the expression vector were incubated in 50 mL LB cultures supplemented with 100 µg/mL of ampicillin at 37 °C overnight with shaking at 160 rpm. Aliquots (25 mL) of the overnight culture were used to inoculate 1 L of supplemented LB media, which was grown to an OD_{600} of 0.6 – 0.8 by incubation at 37 °C with shaking. IPTG (1 mM) was used to induce protein expression and the expression culture was incubated at 25 °C for 20 h with shaking. The cells were harvested by centrifugation ($5000 \times g$, 30 min, 4 °C) and the pellets stored at -30 °C.

6.2.3.7 Protein Purification

Pelleted cells (Section 6.2.3.5 and Section 6.2.3.6) were thawed on ice, resuspended in 20 mL of Buffer A and sonicated as explained in Section 6.2.3.5. The resulting lysate was then centrifuged ($14000 \times g$, 30 min, 4 °C) and filtered to 0.45 µm, after which it was loaded onto a 5 mL IMAC column that had been pre-equilibrated with Buffer A (Table 8). Unbound proteins were eluted with 10 column volumes of Buffer A (Table 8). His-tagged proteins were eluted over a 0 – 100% gradient of Buffer B (Table 8). Protein elution was monitored by measuring the absorbance at 280 nm, with peak fractions examined by SDS-PAGE (Section

6.2.1.5). The fractions estimated to contain >95% pure PaDAPEP were pooled and dialysed into Buffer C overnight at 4 °C. Purified protein was snap frozen in liquid nitrogen and stored at -80 °C.

Table 8. Protein purification buffers.

Buffer	Components
A	20 mM tris, 500 mM NaCl, 20 mM imidazole, pH 8.0
B	20 mM tris, 500 mM NaCl, 500 mM imidazole, pH 8.0
C	20 mM tris, 150 mM NaCl, 1 mM DTT, pH 8.0

6.2.4 Enzyme Kinetics

6.2.4.1 Rate versus Enzyme Concentration Assay

To measure the enzymatic activity of PaDAPEP, the DAPEP-DAPDH coupled assay was employed as previously described (Cox *et al*, 2002). Assays were performed in triplicate in 1 mL acrylic cuvettes (pathlength 1 cm) using a Cary 4000 UV/vis spectrophotometer (Agilent). A molar excess of DAPDH, $NADP^+$ and L,L-DAP was maintained to ensure limiting concentrations of PaDAPEP were responsible for the measured rate of the reaction. Assay reagents (Table 9) were incubated at 37 °C for 10 min prior to initiation of the reaction with PaDAPEP. Initial rate was measured by monitoring the decrease in absorbance at 340 nm due to the reduction of $NADP^+$ as a function of time.

Table 10. DAPEP-DAPDH assay components.

Component	Concentration (mM)	Volume per reaction (µL)
Tris	100	40
DTT	1	80
NADP$^+$	0.5	40
DAPDH	0.002	92
L,L-DAP	-*	-*
PaDAPEP	-*	-*
MQ Water	-	Fill to 800

*varied depending on assay.

6.2.4.2 Michaelis-Menten Analysis

The Michaelis-Menten parameters were determined by employing a modified version of the assay described in Section 6.2.7.1. Specifically, PaDAPEP concentration was fixed at 63 nM within the reaction, while L,L-DAP concentration was titrated at varying concentrations (16 µM – 2 mM). The data were fitted to the Michaelis-Menten model (Equation 1) using GraphPad Prism (version 8.4.3).

Equation 1:

$$V_0 = \frac{V_{\max} \times [S]}{K_{\mathrm{m}} + [S]}$$

Where: V_0 = Initial rate

K_{m} = Michaelis-Menten constant

$V_{\max}$ = Maximum reaction rate

[S] = Substrate concentration

6.2.5 Structural Characterisation

6.2.5.1 Circular Dichroism Spectroscopy

The secondary structure of PaDAPEP was assessed by CD spectroscopy using an AvivBiomedical Model 420 CD spectrometer. The wavelength spectrum was measured using 20 mM NaH_2PO_4, 50 mM KF buffer, pH 8.0 at 0.15 mg/mL of protein in a 1 mm quartz cuvette and at a slit bandwidth of 1 nm. Measurements were taken every 1 nm between 190 – 260 nm with a signal average time of 5 s at 25 °C. The CONTINLL algorithm employing the SP29 reference set was applied to analyse the data, which was retrieved from the CDPro software package (Sreerama *et al*, 1999; Sreerama & Woody, 2000).

6.2.5.2 Analytical Ultracentrifugation

The oligomeric state of PaDAPEP in solution was determined by AUC using a ProteomeLab^{TM} XL-A analytical ultracentrifuge (Beckman Coulter) as previously described (Burgess *et al*, 2008). Solvent density, solvent viscosity and estimates of the partial specific volume were calculated using SEDNTERP (Laue *et al*, 1992). A sedimentation velocity experiment was conducted using an 8-hole An50-Ti analytical rotor to hold double sector centrifuge cells that were assembled with either sapphire or quartz windows. Each cell was loaded with 400 µL of reference buffer (20 mM tris, 150 mM NaCl, pH 8.0) and 380 µL of protein samples at 0.3 and 0.9 mg/mL. Data were collected at a wavelength of 280 nm, temperature of 20 °C, and rotor speed of 40,000 rpm in continuous mode employing a step size of 0.003 cm without averaging. Data were fitted with a continuous sedimentation coefficient distribution model using SEDFIT (Schuck, 2000).

6.2.5.3 X-ray Crystallography

6.2.5.3.1 Crystallisation

An initial crystallisation screen for PaDAPEP was carried out at C3 (CSIRO, Melbourne). The Shotgun protein crystallisation screen was completed at protein concentrations of 6.0 and 11 mg/mL. Crystal formation was achieved by sitting-drop vapour diffusion at 20 °C, with promising crystallisation conditions being further optimised in-house. Crystals from the inhouse optimisation were grown at 20 °C using the hanging-drop vapour diffusion method. A summary of the crystallisation details can be seen in Tables 10 and 11.

Table 10. Crystallisation condition optimisation of PaDAPEP at 6.0 mg/mL.

25% (w/v) PEG 3350; 0.18 M potassium sodium tartrate; 0.1 M tris chloride, pH 8.2	24% (w/v) PEG 3350; 0.10 M bris-tris chloride, pH 5.5	22% (w/v) PEG 3350; 0.23 M sodium acetate; 0.1 M tris chloride, pH 7.4	22% (w/v) PEG 3350; 0.10 M bis-tris chloride, pH 5.5
19% (w/v) PEG 10000; 0.30 M ammonium sulfate	27% (w/v) PEG 3350; 0.27 M potassium sodium tartrate	28% (w/v) PEG 3350	18% (w/v) PEG 10000; 0.10 M bis-tris chloride, pH 6.0
18% (w/v) PEG 3350; 0.10 M bis-tris chloride, pH 5.9	24% (w/v) PEG 3350; 0.13 M sodium acetate; 0.10 M bis-tris chloride, pH 5.5	19% (w/v) PEG 3350; 0.15 M potassium sodium tartrate; 0.10 M bis-tris chloride, pH 6.4	26% (w/v) PEG 3350; 0.30 M ammonium sulfate; 0.10 M bis-tris chloride, pH 6.2
28% (w/v) PEG 3350; 0.27 M ammonium sulfate	25% (w/v) PEG 3350; 0.10 M bis-tris chloride, pH 5.5	20% (w/v) PEG 3350; 0.20 M potassium sodium tartrate	25% (w/v) PEG 3350; 0.20 M sodium acetate; 0.10 M bis-tris chloride, pH 5.5
20% (w/v) PEG 3350; 0.20 M ammonium sulfate	25% (w/v) PEG 3350; 0.10 M tris chloride, pH 8.5	17% (w/v) PEG 10000; 0.10 M sodium acetate; 0.10 M bis-tris chloride, pH 5.5	18% (w/v) PEG 10000; 0.22 M ammonium sulfate
19% (w/v) PEG 3350; 0.10 M bis-tris chloride, pH 5.7	18% (w/v) PEG 10000; 0.10 M ammonium sulfate	25% (w/v) PEG 3350; 0.20 M ammonium sulfate; 0.10 M bis-tris chloride, pH 6.5	18% (w/v) PEG 10000; 0.084 M ammonium sulfate

Table 11. Crystallisation condition optimisation of PaDAPEP at 11 mg/mL.

20% (w/v) PEG 8000; 0.21 M sodium acetate; 0.10 M bis-tris chloride, pH 5.5	25% (w/v) PEG 3350; 0.10 tris chloride, pH 8.3	17% (w/v) PEG 10000; 0.12 M sodium acetate; 0.1 M bis-tris chloride, pH 5.8	20% (w/v) PEG 8000; 0.10 M sodium acetate; 0.10 M bis-tris chloride, pH 5.5
27% (w/v) PEG 3350; 0.14 M sodium acetate; 0.10 M tris chloride, pH 8.8	26% (w/v) PEG 3350; 0.13 M sodium acetate; 0.10 M bis-tris chloride, pH 5.5	24% (w/v) PEG 3350; 0.28 M ammonium sulfate; 0.10 M sodium MES, pH 6.4	17% (w/v) PEG 10000; 0.10 M sodium acetate; 0.10 M bis-tris chloride, pH 5.5
21% (w/v) PEG 3350; 0.072 M sodium acetate; 0.10 M bis-tris chloride, pH 6.4	17% (w/v) PEG 10000; 0.051 M sodium acetate; 0.10 M tris chloride, pH 8.8	25% (w/v) PEG 3350; 0.10 M bis-tris chloride, pH 5.5	25% (w/v) PEG 3350; 0.20 M ammonium sulfate; 0.10 M tris chloride, pH 8.5
24% (w/v) PEG 3350; 0.15 M sodium acetate; 0.10 M bis-tris chloride, pH 6.3	26% (w/v) PEG 3350; 0.10 M sodium HEPES, pH 6.6	25% (w/v) PEG 3350; 0.20 M sodium acetate; 0.10 M bis-tris chloride, pH 5.5	22% (w/v) PEG 3350; 0.20 M ammonium sulfate; 0.10 M tris chloride, pH 8.5
19% (w/v) PEG 8000; 0.26 M sodium acetate; 0.10 M tris chloride, pH 7.8	27% (w/v) PEG 3350; 0.11 M sodium acetate; 0.10 M bis-tris chloride, pH 5.5	25% (w/v) PEG 3350; 0.20 M ammonium sulfate; 0.10 M sodium HEPES, pH 7.5	28% (w/v) PEG 3350; 0.085 M sodium acetate; 0.10 M bis-tris chloride, pH 5.5
21% (w/v) PEG 3350; 0.23 M sodium acetate; 0.10 M sodium MES, pH 5.9	26% (w/v) PEG 3350; 0.28 M sodium acetate; 0.10 M sodium HEPES, pH 7.1	25% (w/v) PEG 3350; 0.20 M ammonium sulfate; 0.10 M bis-tris chloride, pH 6.5	25% (w/v) PEG 3350; 0.28 M sodium acetate; 0.10 M bis-tris chloride, pH 5.7

Reservoir solutions were prepared to contain 0.28 M ammonium sulfate, 24% (w/v) PEG 3350 and 0.10 M sodium MES (pH 6.4). Protein (11 mg/mL) was crystallised in an apo form at 20 °C. Crystals were transferred to cryo-protectant (24% [w/v] PEG 3350, 0.28 M ammonium sulfate, 0.10 M sodium MES [pH 6.4], 20% [v/v] glycerol) before being flash frozen in liquid nitrogen. X-ray diffraction data were collected at 100 K using an EIGER 16M detector with 20% beam attenuation on the MX2 beamline (Aragão *et al*, 2018) at the Australian Synchrotron (Monash University, Clayton).

X-ray data were integrated with XDS (Kabsch, 2010) and scaled using AIMLESS (Evans & Murshudov, 2013). The crystal structure was solved by molecular replacement using AUTORICKSAW (Panjikar *et al*, 2005) with *A. thaliana* DAPEP (PDB ID: 3EKM) as a search model. Structural refinements were completed using PHENIX.REFINE (Afonine *et al*, 2012) and model building was performed with COOT (Emsley *et al*, 2010). The structure was refined using a TLS rigid-body motion refinement with 5 groups established using the TLSMD server (Painter & Merritt, 2006). Structure quality was assessed in COOT and the online PDB validation tool.

References

Afonine PV, Grosse-Kunstleve RW, Echols N, Headd JJ, Moriarty NW, Mustyakimov M, Terwilliger TC, Urzhumtsev A, Zwart PH & Adams PD (2012) Towards automated crystallographic structure refinement with phenix.refine. *Acta Cryst D* **68**: 352–367

Alm RA & Lahiri SD (2020) Narrow-spectrum antibacterial agents – benefits and challenges. *Antibiotics (Basel)* **9:** 418

Aminov RI (2010) A brief history of the antibiotic era: lessons learned and challenges for the future. *Front Microbiol* **1:** 134

Aparicio T, Lorenzo V de & Martínez-García E (2019) CRISPR/Cas9-enhanced ssDNA recombineering for *Pseudomonas putida*. *Microb Biotechnol* 1**2:** 1076–1089

Aragão D, Aishima J, Cherukuvada H, Clarken R, Clift M, Cowieson NP, Ericsson DJ, Gee CL, Macedo S, Mudie N, *et al* (2018) MX2: a high-flux undulator microfocus beamline serving both the chemical and macromolecular crystallography communities at the Australian Synchrotron. *J Synchrotron Rad* **25:** 885–891

Bassetti M, Vena A, Croxatto A, Righi E & Guery B (2018) How to manage *Pseudomonas aeruginosa* infections. *Drugs Context* **7:** 212527

Behrends V, Ryall B, Zlosnik JEA, Speert DP, Bundy JG & Williams HD (2013) Metabolic adaptations of *Pseudomonas aeruginosa* during cystic fibrosis chronic lung infections. *Environ Microbiol* **15:** 398–408

Berman H, Henrick K & Nakamura H (2003) Announcing the worldwide Protein Data Bank. *Nat Struct Mol Biol* **10:** 980–980

Beveridge TJ (2001) Use of the gram stain in microbiology. *Biotech Histochem* **76:** 111–118

Blankenfeldt W, Kuzin AP, Skarina T, Korniyenko Y, Tong L, Bayer P, Janning P, Thomashow LS & Mavrodi DV (2004) Structure and function of the phenazine biosynthetic protein PhzF from *Pseudomonas fluorescens*. *PNAS* **101:** 16431–16436

Burgess BR, Dobson RCJ, Bailey MF, Atkinson SC, Griffin MDW, Jameson GB, Parker MW, Gerrard JA & Perugini MA (2008) Structure and evolution of a novel dimeric enzyme from a clinically important bacterial pathogen. *J Biol Chem* **283:** 27598–27603

Buschiazzo A, Goytia M, Schaeffer F, Degrave W, Shepard W, Grégoire C, Chamond N, Cosson A, Berneman A, Coatnoan N, *et al* (2006) Crystal structure, catalytic mechanism, and mitogenic properties of *Trypanosoma cruzi* proline racemase. *PNAS* **103:** 1705–1710

Caplan JF, Zheng R, Blanchard JS & Vederas JC (2000) Vinylogous amide analogues of diaminopimelic acid (DAP) as inhibitors of enzymes involved in bacterial lysine biosynthesis. *Org Lett* **2:** 3857–3860

Centers for Disease Control and Prevention (2013) *Antibiotic resistance threats in the United States.* U.S. Department of Health and Human Services, Atlanta, GA.

Centers for Disease Control and Prevention (2019) *Antibiotic resistance threats in the United States.* U.S. Department of Health and Human Services, Atlanta, GA.

Chuanchuen R, Narasaki CT & Schweizer HP (2002) Benchtop and microcentrifuge preparation of *Pseudomonas aeruginosa* competent cells. *BioTechniques* **33:** 760–763

Cirilli M, Zheng R, Scapin G & Blanchard JS (1998) Structural symmetry: the threedimensional structure of *Haemophilus influenzae* diaminopimelate epimerase. *Biochem* **37:** 16452–16458

Conly J & Johnston B (2005) Where are all the new antibiotics? The new antibiotic paradox. *Can. J Infect Dis Med Microbiol* **16:** 159–160

Cox R, Durston J & I. Roper D (2002) Synthesis and in vitro enzyme activity of an oxa analogue of azi-DAP. *J. Chem Soc Perkin 1* **8:** 1029–1035

Cox RJ, Sutherland A & Vederas JC (2000) Bacterial diaminopimelate metabolism as a target for antibiotic design. *Bioorg Med Chem* **8:** 843–871

Defoirdt T (2018) Quorum-sensing systems as targets for antivirulence therapy. *Trends in Microbiology* **26:** 313–328

Dogovski C, Atkinson S, Dommaraju SR, Hor L, Dobson R, Hutton C, Gerrard J & Perugini M (2009) Lysine biosynthesis in bacteria: An unchartered pathway for novel antibiotic design, Biotechnology Part i. *Encycl Life Support Syst* **11:** 116–136

Emsley P, Lohkamp B, Scott WG & Cowtan K (2010) Features and development of Coot. *Acta Crystallogr D Biol Crystallogr* **66:** 486–501

Evans PR & Murshudov GN (2013) How good are my data and what is the resolution? *Acta Cryst D* **69:** 1204–1214

Falagas ME, Kasiakou SK & Saravolatz LD (2005) Colistin: the revival of polymyxins for the management of multidrug-resistant Gram-negative bacterial infections. *Clin Infect Dis* **40:** 1333–1341

Fleitas Martínez O, Cardoso MH, Ribeiro SM & Franco OL (2019) Recent advances in antivirulence therapeutic strategies with a focus on dismantling bacterial membrane microdomains, toxin neutralization, quorum-sensing interference and biofilm inhibition. *Front Cell Infect Microbiol* **9:** 74

Fleming-Dutra KE, Hersh AL, Shapiro DJ, Bartoces M, Enns EA, File TM, Finkelstein JA, Gerber JS, Hyun DY, Linder JA, *et al* (2016) Prevalence of inappropriate antibiotic prescriptions among U.S. ambulatory care visits, 2010-2011. *JAMA* **315:** 1864–1873

Friedman ND, Temkin E & Carmeli Y (2016) The negative impact of antibiotic resistance. *Clinical Microbiology and Infection* **22:** 416–422

Garvey GS, Rocco CJ, Escalante-Semerena JC & Rayment I (2007) The three-dimensional crystal structure of the PrpF protein of *Shewanella oneidensis* complexed with transaconitate: Insights into its biological function. *Protein Sci* **16:** 1274–1284

Grassick A, Sulzenbacher G, Roig-Zamboni V, Campanacci V, Cambillau C & Bourne Y (2004) Crystal structure of *Escherichia coli* yddE protein reveals a striking homology with diaminopimelate epimerase. *Proteins* **55:** 764–767

Hmelo LR, Borlee BR, Almblad H, Love ME, Randall TE, Tseng BS, Lin C, Irie Y, Storek KM, Yang JJ, *et al* (2015) Precision-engineering the *Pseudomonas aeruginosa* genome with two-step allelic exchange. *Nat Protoc* **10:** 1820–1841

Hor L, Dobson RCJ, Downton MT, Wagner J, Hutton CA & Perugini MA (2013) Dimerization of bacterial diaminopimelate epimerase is essential for catalysis. *J Biol Chem* **288:** 9238–9248

Huang W & Wilks A (2017) A rapid seamless method for gene knockout in *Pseudomonas aeruginosa. BMC Microbiol* **17:** 199

Hutchings MI, Truman AW & Wilkinson B (2019) Antibiotics: past, present and future. *Curr Opin Microbiol* **51:** 72–80

Hutton CA, Perugini MA & Gerrard JA (2007) Inhibition of lysine biosynthesis: an evolving antibiotic strategy. *Mol BioSyst* **3:** 458–465

Iwasaki K, Uchiyama H, Yagi O, Kurabayashi T, Ishizuka K & Takamura Y (1994) Transformation of *Pseudomonas putida* by electroporation. *Biosci Biotechnol Biochem* **58:** 851–854

Kabsch W (2010) XDS. *Acta Cryst D* **66:** 125–132

Kapoor G, Saigal S & Elongavan A (2017) Action and resistance mechanisms of antibiotics: A guide for clinicians. *J Anaesthesiol Clin Pharmacol* **33:** 300–305

Kollef MH (2008) Broad-spectrum antimicrobials and the treatment of serious bacterial infections: getting it right up front. *Clin Infect Dis* **47:** S3–S13

Koo CW & Blanchard JS (1999) Chemical mechanism of *Haemophilus influenzae* diaminopimelate epimerase. *Biochem* **38:** 4416–4422

Kos VN, McLaughlin RE & Gardner HA (2016) Identification of unique in-frame deletions in OprD among clinical isolates of *Pseudomonas aeruginosa. Pathog Dis* **74**

Landers TF, Cohen B, Wittum TE & Larson EL (2012) A review of antibiotic use in food animals: perspective, policy, and potential. *Public Health Rep* **127:** 4–22

Landini P, Antoniani D, Burgess JG & Nijland R (2010) Molecular mechanisms of compounds affecting bacterial biofilm formation and dispersal. *Appl Microbiol Biotechnol* **86:** 813–823

Laue TM, Shah BD, Ridgeway TM & Pelletier SL (1992) Computer-aided interpretation of analytical sedimentation data for proteins. In *Analytical Ultracentrifugation in Biochemistry and Polymer Science*, Harding SE & Rowe AJ (eds) pp 90–125. The Royal Society of Chemistry, Cambridge

Liger D, Quevillon-Cheruel S, Sorel I, Bremang M, Blondeau K, Aboulfath I, Janin J, van Tilbeurgh H & Leulliot N (2005) Crystal structure of YHI9, the yeast member of the phenazine biosynthesis PhzF enzyme superfamily. *Proteins* **60:** 778–786

Lister PD, Wolter DJ & Hanson ND (2009) Antibacterial-resistant *Pseudomonas aeruginosa*: clinical impact and complex regulation of chromosomally encoded resistance mechanisms. *Clin Microbiol Rev* **22:** 582–610

Lloyd AJ, Huyton T, Turkenburg J & Roper DI (2004) Refinement of *Haemophilus influenzae* diaminopimelic acid epimerase (DapF) at 1.75 A resolution suggests a mechanism for stereocontrol during catalysis. *Acta Crystallogr D Biol Crystallogr* **60:** 397–400

Lockhart DEA, Stanley M, Raimi OG, Robinson DA, Boldovjakova D, Squair DR, Ferenbach AT, Fang W & van Aalten DMF (2020) Targeting a critical step in fungal hexosamine biosynthesis. *J Biol Chem* **295:** 8678–8691

Magiorakos A-P, Srinivasan A, Carey RB, Carmeli Y, Falagas ME, Giske CG, Harbarth S, Hindler JF, Kahlmeter G, Olsson-Liljequist B, Paterson DL, Rice LB, Stelling J, Struelens MJ, Vatopoulos A, Weber JT & Monnet DL (2012) Multidrug-resistant, extensively drug-resistant and pandrug-resistant bacteria: an international expert proposal for interim standard definitions for acquired resistance. *Clin Microbiol Infect* **18:** 268–281

Mao F, Dam P, Chou J, Olman V & Xu Y (2009) DOOR: a database for prokaryotic operons. *Nucleic Acids Res* **37:** D459-463

Margolin W (2018) Bacterial Cell Wall. In *eLS* pp 1–11. John Wiley & Sons, Ltd: Chichester

Mayclin SJ, Lorimer DD & Edwards TE (2015) Structure of a diaminopimelate epimerase from *Acinetobacter baumannii* doi: 10.2210/pdb5HA4/pdb

Meletis G & Bagkeri M (2013) *Pseudomonas aeruginosa*: multi-drug-resistance development and treatment options. In Basak S (eds.), *Infection Control* pp 33–56. InTech Open Access Publisher, London.

Mielko KA, Jabłoński SJ, Milczewska J, Sands D, Łukaszewicz M & Młynarz P (2019) Metabolomic studies of *Pseudomonas aeruginosa*. *World J Microbiol Biotechnol* **35:** 178

Moradali MF, Ghods S & Rehm BHA (2017) *Pseudomonas aeruginosa* lifestyle: a paradigm for adaptation, survival, and persistence. *Front Cell Infect Microbiol* **7:** 39

Munita JM & Arias CA (2016) Mechanisms of antibiotic resistance. *Microbiol Spectr* **4**

Nguyen L, Garcia J, Gruenberg K & MacDougall C (2018) Multidrug-resistant *Pseudomonas* infections: hard to treat, but hope on the horizon? *Curr Infect Dis Rep* **20:** 23

O'Neill J (2014) Antimicrobial Resistance: Tackling a crisis for the health and wealth of nations. *Rev Antimicrob Resist* Available at: http://amr-review.org/Publications

Painter J & Merritt EA (2006) TLSMD web server for the generation of multi-group TLS models. *J Appl Cryst* **39:** 109–111

Pang Z, Raudonis R, Glick BR, Lin T-J & Cheng Z (2019) Antibiotic resistance in *Pseudomonas aeruginosa*: mechanisms and alternative therapeutic strategies. *Biotechnol Adv* **37:** 177–192

Panjikar S, Parthasarathy V, Lamzin VS, Weiss MS & Tucker PA (2005) Auto-Rickshaw: an automated crystal structure determination platform as an efficient tool for the validation of an X-ray diffraction experiment. *Acta Cryst D* **61:** 449–457

Park JS, Lee WC, Song JH, Kim SI, Lee JC, Cheong C & Kim H-Y (2013) Purification, crystallization and preliminary X-ray crystallographic analysis of diaminopimelate epimerase from *Acinetobacter baumannii*. *Acta Cryst F* **69:** 42–44

Parsons JF, Song F, Parsons L, Calabrese K, Eisenstein E & Ladner JE (2004) Structure and function of the phenazine biosynthesis protein PhzF from *Pseudomonas fluorescens*. *Biochem* **43:** 12427–12435

Pillai B, Cherney M, Diaper CM, Sutherland A, Blanchard JS, Vederas JC & James MNG (2007) Dynamics of catalysis revealed from the crystal structures of mutants of diaminopimelate epimerase. *Biochem Biophys Res Commun* **363:** 547–553

Pillai B, Cherney MM, Diaper CM, Sutherland A, Blanchard JS, Vederas JC & James MNG (2006) Structural insights into stereochemical inversion by diaminopimelate epimerase: An antibacterial drug target. *PNAS* **103:** 8668–8673

Renwick M & Mossialos E (2018) What are the economic barriers of antibiotic R&D and how can we overcome them? *Expert Opin Drug Discov* **13:** 889–892

Rosenblatt-Farrell N (2009) The Landscape of Antibiotic Resistance. *Environ Health Perspect* **117:** 244–250

Sagong HY & Kim KJ (2017) Structural basis for redox sensitivity in *Corynebacterium glutamicum* diaminopimelate epimerase: an enzyme involved in l -lysine biosynthesis. *Sci Rep* **7:** 42318

Sambrook JF & Russel DW (2001) Molecular cloning: a laboratory manual 3rd ed. Cold Spring Harbor, NY: Cold Spring Harbor Laboratory Press

dos Santos ALS, Galdino ACM, de Mello TP, Ramos L de S, Branquinha MH, Bolognese AM, Columbano J & Roudbary M (2018) What are the advantages of living in a community? A microbial biofilm perspective! *Mem Inst Oswaldo Cruz* **113:** e180212

Sarkar P, Yarlagadda V, Ghosh C & Haldar J (2017) A review on cell wall synthesis inhibitors with an emphasis on glycopeptide antibiotics. *Med chem comm* **8:** 516–533

Schuck P (2000) Size-distribution analysis of macromolecules by sedimentation velocity ultracentrifugation and lamm equation modeling. *Biophys J* **78:** 1606–1619

Sengupta S, Chattopadhyay MK & Grossart H-P (2013) The multifaceted roles of antibiotics and antibiotic resistance in nature. *Front Microbiol* **4:** 47

Shen H, Han F, Lin Y & Yu W (2006) A high efficient electroporation of *Pseudomonas sp.* QDA pretreated with alginate lyase. *Enzyme Microb Tech* **39:** 677–682

Silhavy TJ, Kahne D & Walker S (2010) The bacterial cell envelope. *Cold Spring Harb Perspect Biol* **2:** a000414

Spellberg B & Gilbert DN (2014) The future of antibiotics and resistance: a tribute to a career of leadership by John Bartlett. *Clin Infect Dis* **59:** S71–S75

Sreerama N, Venyaminov SY & Woody RW (1999) Estimation of the number of alpha-helical and beta-strand segments in proteins using circular dichroism spectroscopy. *Protein Sci* **8:** 370–380

Sreerama N & Woody RW (2000) Estimation of protein secondary structure from circular dichroism spectra: comparison of CONTIN, SELCON, and CDSSTR methods with an expanded reference set. *Anal Biochem* **287:** 252–260

Swift S, Throup JP, Williams P, Salmond GPC & Stewart GSAB (1996) Quorum sensing: a population-density component in the determination of bacterial phenotype. *Trends Biochem Sci* **21:** 214–219

Usha V, Dover LG, Roper DI, Fütterer K & Besra GS (2009) Structure of the diaminopimelate epimerase *dapF* from *Mycobacterium tuberculosis*. *Acta Crystallogr D Biol Crystallogr* **65:** 383–387

Usha V, Dover LG, Roper DL & Besra GS (2008) Characterization of *Mycobacterium tuberculosis* diaminopimelic acid epimerase: paired cysteine residues are crucial for racemization. *FEMS Microbiol Lett* **280:** 57–63

Van Boeckel TP, Pires J, Silvester R, Zhao C, Song J, Criscuolo NG, Gilbert M, Bonhoeffer S & Laxminarayan R (2019) Global trends in antimicrobial resistance in animals in low- and middle-income countries. *Sci* **365:** 5649–5654

Velarde M, Macieira S, Hilberg M, Bröker G, Tu S-M, Golding BT, Pierik AJ, Buckel W & Messerschmidt A (2009) Crystal structure and putative mechanism of 3methylitaconate-delta-isomerase from *Eubacterium barkeri*. *J Mol Biol* **391:** 609–620

Venter H, Mowla R, Ohene-Agyei T & Ma S (2015) RND-type drug efflux pumps from Gramnegative bacteria: molecular mechanism and inhibition. *Front Microbiol* **6:** 377

Ventola CL (2015) The antibiotic resistance crisis. *Pharm Ther* **40:** 277–283

Venturi V (2006) Regulation of quorum sensing in *Pseudomonas*. *FEMS Microbiol Rev* **30:** 274–291

Vollmer W, Blanot D & De Pedro MA (2008) Peptidoglycan structure and architecture. *FEMS Microbiol Rev* **32:** 149–167

Welte W, Nestel U, Wacker T & Diederichs K (1995) Structure and function of the porin channel. *Kidney Int* **48:** 930–940

White PJ, Lejeune B & Work E (1969) Assay and properties of diaminopimelate epimerase from *Bacillus megaterium*. *Biochem J* **113:** 589–601

World Health Organisation ed. (2014) *Antimicrobial resistance: global report on surveillance.* World Health Organization, Geneva, Switzerland

Yang JJ, Wang JT, Cheng A, Chuang YC & Sheng WH (2018) Impact of broad-spectrum antimicrobial treatment on the ecology of intestinal flora. *J Microbiol Immunol Inf* **51:** 681–687

Zhao L & Chmielewski J (2013) Inhibition of HIV-1 integrase dimerization and activity with crosslinked interfacial peptides. *Bioorg Med Chem* **21:** 4041–4044